Physics of Plasmas ARTICLE scitation.org/journal/php

Linear ion-scale microstability analysis of high and low-collisionality NSTX discharges and NSTX-U projections

Cite as: Phys. Plasmas **29**, 102303 (2022); doi: 10.1063/5.0102169
Submitted: 7 June 2022 · Accepted: 22 September 2022 ·
Published Online: 31 October 2022 · Publisher error corrected: 9 November 2022

C. F. Clauser,[1,a)] W. Guttenfelder,[2] T. Rafiq,[1] and E. Schuster[1]

AFFILIATIONS

[1]Lehigh University, Bethlehem, Pennsylvania 18015, USA
[2]Princeton Plasma Physics Laboratory, Princeton, New Jersey 08540, USA

[a)]Author to whom correspondence should be addressed: cclauser@lehigh.edu

ABSTRACT

Linear gyrokinetic simulations were conducted to investigate ion-gyroradius-scale micro-instability predictions for high-beta NSTX discharges and NSTX-U projections that span over an order of magnitude variation in collisionality. A complex mix of microtearing modes and hybrid trapped electron modes/kinetic ballooning modes (TEM/KBM) is predicted for all experimental or projected conditions. Ion temperature gradient (ITG) instabilities are typically stable in the NSTX discharges investigated, consistent with the observed neoclassical ion thermal transport. ITG thresholds inferred from the simulations are typically much higher than the experimental NSTX gradients, as well as the projected gradients in the NSTX-U scenario, which assumed ion temperatures limited by neoclassical transport only. The analysis suggests ITG instabilities are unlikely to contribute significant anomalous thermal losses in high-beta, lower collisionality NSTX-U scenarios. On the other hand, the NSTX experimental profiles and NSTX-U projections are predicted to be very close to the predicted onset of unstable KBM at most radii investigated. The proximity of the various discharges to the KBM instability threshold implies it may play an important role in setting profile shapes and limiting global energy confinement. It remains to be understood and predicted how KBM contributes to multichannel transport (thermal and particle transport, for both ions and electrons) in a way that is consistent with experimental inferences.

I. INTRODUCTION

NSTX high-β H-mode discharges have ion thermal transport near neoclassical levels,[1,2] implying negligible turbulent contributions to ion thermal losses. This observation is consistent with the stabilization of ion temperature gradient (ITG) turbulence that is predicted to occur in high-β, low aspect ratio (R/a) configurations due to (i) reduced "bad curvature" drive from highly shaped flux surfaces (low R/a, high elongation and triangularity) and large Shafranov shift,[3–5] (ii) weakened or reversed trapped particle precession that minimizes trapped electron resonances,[4] and (iii) coupling to magnetic fluctuations at increasing β.[6] Any ITG modes that may remain linearly unstable are often expected to be suppressed by perpendicular $E \times B$ flow shear,[7] which can be large in NSTX due to the injected torque from NBI heating and relatively small moment of inertia. In contrast, electron thermal transport has been almost always found to be anomalous, in which electron temperature gradient (ETG) modes or microtearing modes (MTMs) have been reported to dominate or contribute significantly in certain conditions.[8,9] In the case of ETG modes, the $E \times B$ flow shear is not usually enough to suppress the mode as compared to ITG.[8]

Data from NSTX discharges suggest a scaling of the normalized energy confinement time nearly inverse to the collisionality, ν^*.[10,11] This was one of the main motivations for exploring lower collisionality regimes in the NSTX-U device[10,12] in which collisionalities up to six times lower than those obtained in NSTX are expected to be reached in order to confirm this trend. Limited observations indicated that ion thermal and impurity transport coefficients were beginning to deviate from neoclassical predictions in the lowest collisionality NSTX H-mode discharges.[11,13] Therefore, it is of primary interest to determine whether turbulent ion transport will become increasingly relevant in those regimes and if its presence will impact thermal or particle transport. In particular, it is important to find whether ion temperature gradient modes (ITGs), trapped electron modes (TEMs), or kinetic ballooning modes (KBMs) will be dominant in those regimes.

As a first step in addressing the relevance and role of these modes in such conditions, a broad series of linear gyrokinetics (GK)

simulations on NSTX and NSTX-U equilibria are conducted to identify all the modes present in the ion-scale wavenumber range, including ion-directed modes such as KBMs or ITGs, as well as electron-directed modes such as TEMs or MTMs. In addition, scans to determine primarily the stability thresholds of ion-directed modes were also conducted. The work is focused on the core transport region, leaving the pedestal region out of the scope. In the first part of this work, three different NSTX discharges with high, medium, and low collisionalities are selected. For each discharge, several scans are performed over the ion scale wavelength range, varying the normalized wavenumber, at different minor radii within the confinement region. Additional parameters, such as the normalized ion temperature gradient and plasma beta, were also scanned to help to determine the different modes present and stability thresholds. In the second part, a similar analysis for an NSTX-U projection is conducted, choosing specifically a scenario predicted to have one of the lowest accessible collisionalities in H-modes. This is the first comprehensive analysis of linear gyrokinetic stability for projected future NSTX-U high-performance H-mode plasmas, a necessary first step toward predicting theoretical transport characteristics. For each discharge, diagrams of the parameter region that was scanned in the ion-range scale, showing the dominant mode along with KBM and ITG thresholds, are presented.

All the simulations are conducted with the CGYRO code,[14] which is part of the GACODE Suite package.[15] CGYRO is an Eulerian GK solver specifically designed and optimized for collisional, electromagnetic and multiscale simulation. It uses field-aligned space coordinates and it is fully spectral in the perpendicular (radial and binormal) directions. The velocity space is represented by the particle speed and pitch angle, allowing for more accurate treatment of the collision operator. Throughout this work, the Sugama operator model[16] implemented in CGYRO is employed. Flux surface shapes are given by the extended Miller's parametrization[17] of the general numerical equilibrium[18] resulting from EFIT reconstructions. In addition, CGYRO can solve a fully electromagnetic GK model, meaning that the perturbed electrostatic potential, parallel vector potential, and parallel magnetic field ($\delta\varphi$, $\delta A_\parallel$, $\delta B_\parallel$) are computed. This is important in order to accommodate electromagnetic effects that arise in high-β conditions such as those present in NSTX and NSTX-U H-modes. Unless it is explicitly indicated, all the simulations presented in this work were conducted using the fully electromagnetic GK model. Reduced electromagnetic GK model, which sets $\delta B_\parallel = 0$, as well as the electrostatic model (ES), which only solves for $\delta\varphi$, are also available in CGYRO and their use in this work will be explicitly indicated.

Although it can be included self-consistently, here the $E \times B$ flow shear, γ_E, is excluded in the linear analysis. In addition, three gyrokinetic species (deuterium, carbon, electrons) are considered. As mentioned above, the present analysis focuses on the ion-scale wavenumber range, defined here by $k_\theta \rho_s \leq 1$. Here, θ is the binormal coordinate, $\rho_s = (m_D T_e)^{1/2}/B_{unit}$ is an effective ion-sound gyroradius and B_{unit} is an effective magnetic field[18,19] (also, see the Appendix for additional details).

Many modes are found to be present throughout the different discharges and scans, such as MTMs, TEMs, KBMs, ITGs, and hybrid TEM/KBM modes. The criteria that are used in this study to identify these modes can be summarized as follows:[20] MTMs present negative real frequency close to electron diamagnetic drift frequency, ω_{*e}, tearing parity in the eigenfunctions (odd parity in $\delta\varphi$ and even parity in $\delta A_\parallel$) and they are basically insensitive to $\delta B_\parallel$. In addition, they have large normalized parallel electric field,

$$\hat{E}_\parallel = \frac{\int dz|-\partial_z\delta\varphi + i\omega\delta A_\parallel|}{\int dz|\partial_z\delta\varphi| + |i\omega\delta A_\parallel|},$$

which is a measure of the ideal-MHD behavior of the mode[21] (here z is a coordinate parallel to the background magnetic field). They are also stabilized when reducing the electron plasma beta. Microtearing modes give magnetic reconnection even if they are tearing-mode stable (see, for example, Ref. 22 and references therein). Additional features of MTMs include the sensitivity to the electron temperature gradient, which in turn drives a large electron-over-ion heat flux ratio.[8,23] KBM modes have positive real frequency (in the ion diamagnetic direction), and their eigenfunctions exhibit ballooning or twisting parity (i.e., even parity in $\delta\varphi$ and odd parity in $\delta A_\parallel$). They present a low $\hat{E}_\parallel$ value, which accounts for the ideal-MHD behavior of KBM modes. They are sensitive to both ion temperature gradients and plasma beta, since they depend ultimately on the total pressure gradient. ITG modes usually present ballooning or twisting parity, with nearly symmetric electrostatic potential, although they can also have a tearing parity branch in some cases.[24,25] ITGs have positive real frequency but, unlike KBMs, they are only sensitive to ion temperature gradients. They also exhibits larger $\hat{E}_\parallel$ values than those observed in KBMs. These are the main differences that are used here to distinguish between KBM and ITG modes. Even though ITG modes are usually introduced as electrostatic modes, their growth rate can be underestimated if electromagnetic effects are not properly taking into account.[26,27] Therefore, it is not assumed that they must be electrostatic. Finally, TEM modes are identified as those modes which do not fit in the previous categories. They can exhibit both positive and negative real frequency, present an even parity in the electrostatic potential, they are almost insensitive to the ion temperature gradient, usually slightly sensitive to the plasma β, and can be destabilized by the electron density gradient. They also present large $\hat{E}_\parallel$ values. In addition to these modes that can be found alone, hybrid TEM/KBM modes often arise in these discharges. They are usually identified when a scan does not show a clear transition from a TEM mode to a KBM, and they exhibit full electromagnetic properties. Many of these properties, as well as other features, have been also presented in Ref. 28, where different properties or features included experimental signals, called "fingerprints," can lead to the identification of the modes. In this work, however, all the analysis to identify the different modes comes from the linear gyrokinetic simulations.

This paper is organized as follows: Sec. II encompass the three NSTX cases, which results are presented in Secs. II A–II C, respectively, and summarized in Sec. II D. Section III presents the results of the selected NSTX-U projection and, finally, Sec. IV presents a summary and conclusions.

II. NSTX CASES

Three different NSTX discharges were selected in this study, and their kinetic profiles, density, and temperature are shown in Fig. 1. The discharges are referred to as high, medium, and low collisionality. This distinction is for the purpose of classifying them in a very simple way. Figure 1(a) shows the high collisionality discharge, which is shot

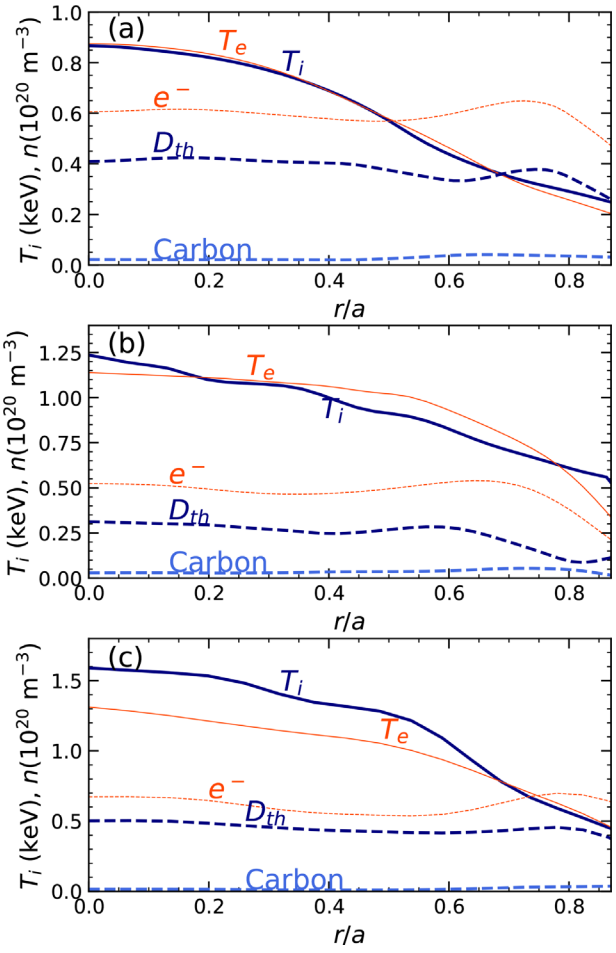

FIG. 1. Temperature and density profiles of the NSTX discharges considered in this study: (a) Shot No. 120 968 at 560 ms, which is referred to as the high collisionality case. (b) Shot No. 129 041 at 490 ms, which is referred to as the medium collisionality case, and (c) Shot No. 120 982 at 620 ms, referred to as the low collisionality NSTX discharge.

#120 968 at 560 ms (TRANSP ID 120968*A*02).[8,22,29] Figure 1(b) shows the medium collisionality discharge, which is shot #129 041 at 490 ms (TRANSP ID 129041*A*10),[9] and Fig. 1(c) shows the low collisionality discharge, which is shot #120 982 at 620 ms (TRANSP ID 120982*A*09). Additional relevant data, at the radial positions, r/a, that are considered in this work, are presented in Table I.

Here, κ is the elongation, δ is the triangularity, q is the safety factor, s is the magnetic shear, $\beta_{e,unit}$ is an effective electron beta, T_i/T_e is the ion–electron temperature ratio, and a/L_{T_x} and a/L_{n_x} are the normalized temperature and density gradients, respectively (here, $x = e, i$ denotes electrons and ions, respectively, and a is the a measure of minor radius). The $\alpha_{MHD,unit}$ is a generalization of the standard MHD α parameter, Z_{eff} is the effective charge, $\nu^{e/i}$ is the electron–ion collision frequency (taking into account Z_{eff}), and $\gamma_E = (r/q)d\omega_0/\,dr\,[c_s/a]$ is the $E \times B$ shearing rate ($\omega_0 = E_r/RB_{pol}$ is taken as the plasma angular frequency profile). Frequencies and growth rates are given in units of c_s/a, where c_s is the ion sound speed evaluated at the electron temperature. A description of some of these quantities is provided in the Appendix, and they were also introduced in great detail in Refs. 5 and 14. In this work, scans over $\beta_{e,unit}$ and a/L_{T_i} are widely conducted and they are done by scaling these parameters in the GK equation implemented in CGYRO.[14] These discharges were also used in previous work that focused, for example, on electron thermal transport[9] or microtearing stability analysis.[22] Here, as mentioned before, the focus is to determine the modes present in the ion-scale region and the thresholds of ITGs or KBMs, if any.

From Fig. 1, it can be observed that the overall temperature increases from the high to the low collisionality discharge, as expected. However, since these equilibria are obtained from real discharges, many other parameters vary as well. For example, the low collisionality discharge is also, in general, a lower $\beta_{e,unit}$ discharge. This, in turn, makes a direct comparison much more challenging.

A. NSTX: High collisionality

The first discharge considered in this study is the high collisionality case. Figure 2 shows the (a) real frequency, ω_r, and (b) growth rate, γ, of modes as a function of the normalized wavenumber, $k_\theta\rho_s$, in the ion-scale range ($k_\theta\rho_s \sim 0.05$–1.0). These results were obtained using the experimental conditions presented in Fig. 1(a) and at the different minor radii indicated in Table I. For each minor radius, the electron diamagnetic frequency, $\omega_{*e} = k_\theta\rho_s\,(a/L_{n_e} + a/L_{T_e})\,[c_s/a]$, and the flow shear rate, γ_E, are included as a reference. The squared-dotted line for $r/a = 0.8$ shows a case in which $\delta B_\parallel$ was turned off in the GK model.

Different modes can be observed, with $r/a = 0.7$ being the most unstable position in which the growth rates greatly exceed γ_E. At $r/a = 0.6$ and 0.7, modes show an approximately linear relation, close to ω_{*e} (negative frequencies are in the electron direction). In addition, even though it is not shown here, turning $\delta B_\parallel$ off for these particular cases does not produce any significant effect. The modes also show tearing parity, as shown, for example, in Fig. 3 where the eigenfunctions for the electrostatic potential, $\delta\varphi$, and the parallel component of the vector potential, $\delta A_\parallel$, are presented as a function of the ballooning angle θ^* for $k_\theta\rho_s = 0.9$ and $r/a = 0.7$. All these features confirm that these modes are MTMs. They are also present at $r/a = 0.5$ for $k_\theta\rho_s > 0.5$ and at $r/a = 0.8$ for $0.2 \lesssim k_\theta\rho_s \lesssim 0.4$. For the latter, it can be observed in Fig. 2 that turning $\delta B_\parallel$ off does not produce any change in that range of wavenumbers.

To determine all the remaining modes at different radial positions, additional scans are required. An example of these scans is shown in Fig. 4 for two minor radii, $r/a = 0.5$ and 0.8. Figure 4 shows (a) and (d) real frequency, (b) and (e) growth rate, and (c) and (f) the normalized parallel electric field. The scans were performed over the normalized ion temperature gradient scale length a/L_{T_i} (indicated with diamond–dashed curves) and over the $\beta_{e,unit}$ parameter (circle-solid curves), but both scans are represented as the change in the $\alpha_{MHD,unit}$ parameter. The scans over ion temperature gradient starts from the experimental value (vertical dotted line), and they are scaled up since the purpose is to see whether ITGs are triggered. The scans over $\beta_{e,unit}$ usually cover values lower and higher than the experimental value.

TABLE I. Summary of relevant data at different minor radius for the different NSTX discharges considered in this work. Kinetic profiles are shown in Fig. 1 for each case.

r/a	κ	δ	q	s	$\beta_{e,unit}$ (%)	T_i/T_e	a/L_{T_e}	a/L_{n_e}	a/L_{T_i}	a/L_{n_i}	$\alpha_{MHD,unit}$	Z_{eff}	$\nu^{e/i}$	γ_E (c_s/a)
(a) High collisionality case: shot No. 120 968 at 560 ms.														
0.5	1.68	0.103	1.37	0.886	3.67	0.987	1.87	−0.106	2.49	1.26	0.474	2.31	1.97	0.220
0.6	1.71	0.127	1.70	1.70	2.51	0.944	2.66	−0.774	2.44	0.686	0.412	2.87	3.91	0.174
0.7	1.76	0.166	2.47	3.16	1.39	1.02	3.11	−0.469	2.05	−1.37	0.416	2.86	7.54	0.118
0.8	1.86	0.237	3.97	3.60	0.588	1.13	2.80	2.60	1.92	3.20	1.28	2.77	11.7	0.0883
(b) Medium collisionality case: shot No. 129 041 at 490 ms.														
0.4	1.49	0.119	1.54	0.373	3.77	0.941	0.365	−0.299	1.19	0.475	0.129	3.22	0.710	0.144
0.5	1.50	0.147	1.72	0.778	3.40	0.894	0.362	−0.713	0.513	−0.970	−0.0880	3.21	0.803	0.0665
0.6	1.54	0.184	2.13	1.45	2.65.	0.888	1.44	−0.545	1.57	1.22	0.392	3.33	1.07	0.163
0.7	1.58	0.235	2.70	1.78	1.70.	0.901	2.07	1.21	1.39	5.19	1.02	4.07	1.80	0.132
0.8	1.63	0.295	3.75	3.30	0.626	1.06	4.95	5.75	1.55	6.72	1.76	4.75	2.78	0.138
(c) Low collisionality case: shot No. 120 982 at 620 ms.														
0.4	2.15	0.170	2.27	0.488	1.90	1.21	0.453	0.398	0.475	0.439	0.300	1.55	0.356	0.119
0.5	2.18	0.207	2.57	0.662	1.52	1.22	0.868	0.141	0.933	0.342	0.387	1.59	0.398	0.219
0.6	2.20	0.244	2.97	0.972	1.17	1.15	1.59	−0.931	2.86	−0.0948	0.543	1.78	0.578	0.297
0.7	2.20	0.282	3.55	1.36	0.933	0.983	2.19	−1.53	3.34	−0.598	0.486	2.23	1.22	0.211
0.8	2.20	0.321	4.43	2.11	0.627	0.941	3.01	0.348	3.00	0.972	1.15	2.41	2.28	0.0932

It is important to note here that the local equilibrium was held fixed during these scans (see the Appendix). The $\alpha_{MHD,unit}$ parameter variation is exclusively for the purpose of combining different parameter scans in the same figure. For clarity, only three different wavenumbers are shown: $k_\theta\rho_s = 0.2$, 0.4, and 0.6.

At $r/a = 0.5$, it can be noted that for $k_\theta\rho_s = 0.4$ and 0.6, there is a clear transition in ω_r, from negative to positive values, along with a sudden drop in $\hat{E}_\parallel$. These changes correspond to a transition from MTM to KBM modes. Under the experimental condition (vertical dotted line), $k_\theta\rho_s = 0.4$ has already transitioned to a KBM while $k_\theta\rho_s = 0.6$ is still an MTM mode very close to the transition to a KBM. On the other hand, $k_\theta\rho_s = 0.2$ shows a mode with a continuous and positive real frequency throughout all the $\alpha_{MHD,unit}$ range. Additional scans (not shown here for simplicity) indicate that, at $\beta_{e,unit} \to 0$ (electrostatic limit), the mode is insensitive to the ion temperature gradient and, hence, identifying it as a TEM. When $\alpha_{MHD,unit}$ increases, a smooth transition in ω_r and $\hat{E}_\parallel$ is observed toward a KBM mode. Even though the normalized electric field has decreased under the experimental condition, it is still falling as $\alpha_{MHD,unit}$ increases. In addition, the growth rate is, under the experimental condition, right at the threshold toward a KBM mode. Therefore, this mode ($k_\theta\rho_s = 0.2$ at $r/a = 0.5$) is referred to as a hybrid TEM/KBM mode under the experimental condition. Hybrid modes have already been reported by different authors.[9,27] Hence, under $r/a = 0.5$ and under the experimental condition, the modes are MTMs for $k_\theta\rho_s > 0.5$, KBM modes for $k_\theta\rho_s = 0.3$ and 0.4, and a hybrid TEM/KBM mode for $k_\theta\rho_s < 0.3$. Increasing either $\beta_{e,unit}$ or a/L_{T_i} triggers KBMs and the similar trend in both scans further confirm that these modes are KBMs since they ultimately depend on pressure gradients, represented here in the $\alpha_{MHD,unit}$ parameter.

Scans at $r/a = 0.8$, see Figs. 4(d)–4(f), reveal KBMs being at their threshold value at low wavenumbers. For example, under the experimental condition and at $k_\theta\rho_s = 0.1$, a transition has already occurred, while at $k_\theta\rho_s = 0.4$, the mode is still an MTM but close to the KBM transition. Modes with $k_\theta\rho_s \geq 0.6$ are identified as TEMs. On one side, these modes have slightly negative real frequencies (in the electron diamagnetic drift direction) under the experimental condition [see Fig. 2(a)] and the growth rate is actually stabilized when either a/L_{T_i} or $\beta_{e,unit}$ is scaled up, before a strong transition to a KBM type occurs. They also exhibit large $\hat{E}_\parallel$. In addition, Fig. 5 shows the eigenfunctions of $k_\theta\rho_s = 0.6$ for three values of the effective electron beta scaling factor, $X_{\beta_{e,unit}}$ (experimental condition corresponds to $X_{\beta_{e,unit}} = 1$). The figure shows that these modes have ballooning or twisting parity. At low $\beta_{e,unit}$, the eigenfunctions are consistent with a TEM mode. As $\beta_{e,unit}$ increases, the mode becomes a KBM, showing a narrower single-peak perturbed electrostatic potential. The change in the phase of the imaginary part of $\delta A_\parallel$, which directly correlates with the associated drop in $\hat{E}_\parallel$, also evidence the transition from one mode to the other. On the other hand, modes with $k_\theta\rho_s \geq 0.6$, as can be noted in Figs. 4(d)–4(f) for $k_\theta\rho_s = 0.6$, present a threshold at $\alpha_{MHD,unit} \approx 1.4$ as $\beta_{e,unit}$ is scaled up, with the growth rate increasing significantly indicating the important role of electromagnetic effects. This is somewhat contrary to standard drift modes like TEMs or ITGs, which have electrostatic limits. However, it has been shown that electromagnetic effects have a significant impact on these modes. In particular, $\delta B_\parallel$ has an important destabilizing effect canceling the self-dug magnetic well that emerges in high-β plasmas.[5,26] This also shown in Fig. 2, in which turning $\delta B_\parallel$ off at $r/a = 0.8$ wipes out the modes with $k_\theta\rho_s \geq 0.6$. However, even though these modes are affected by full electromagnetic effects, they are not well fit as hybrid modes since the transition to a KBM is observed to be very

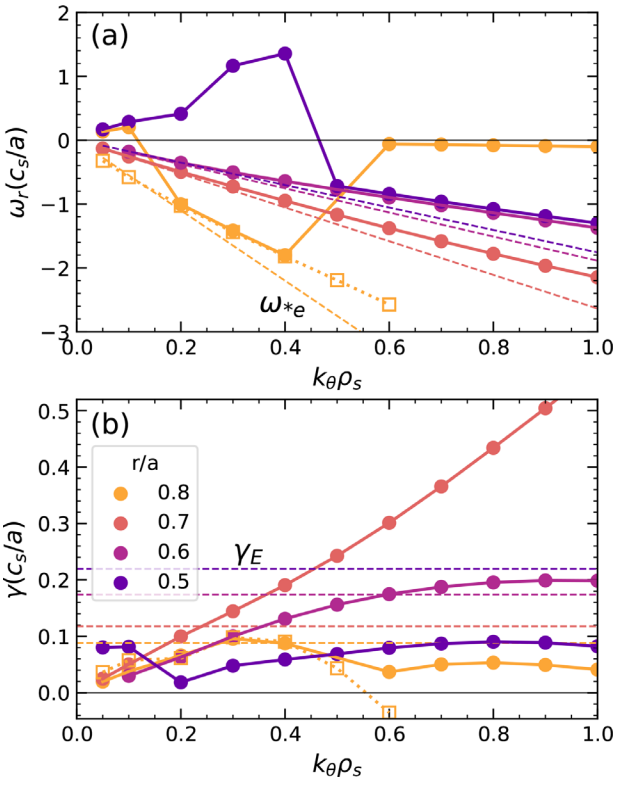

FIG. 2. Analysis of the high collisionality discharge at experimental condition. (a) shows the real frequency, ω_r, and (b) shows the growth rate, γ, both at different minor radius and as a function of the normalized wavenumber $k_\theta\rho_s$. The electron diamagnetic drift frequency, ω_{*e}, and the $E \times B$ flow shear growth rate, γ_E are included as a reference. The squared-dotted line at $r/a = 0.8$ shows a case in which $\delta B_\parallel$ was turned off in the GK model.

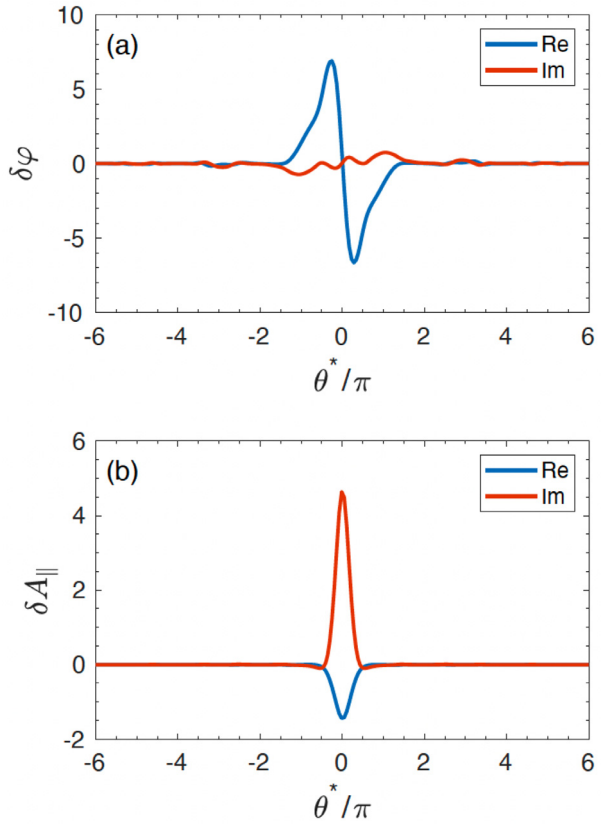

FIG. 3. (a) Perturbed electrostatic potential and (b) parallel component of the perturbed vector potential eigenfunctions, both as a function of the ballooning angle. These eigenfunctions show tearing parity, corresponding to $k_\theta\rho_s = 0.9$ and $r/a = 0.7$ of the NSTX high collisionality discharge (see Fig. 2).

pronounced and, therefore, they are here identified as TEM modes. Hence, at $r/a = 0.8$, the modes present are KBMs at low wavenumbers, followed by MTMs and finally by TEM modes. It is important to remember that, even though the identification of the different modes present is of interest, the dominant modes here are the MTMs and they are the only ones that present $\gamma > \gamma_E$.

The analysis under experimental conditions does not show any ITG mode, as expected for a high collisionality NSTX discharge. The additional scans that helped to determine different modes present, such as those ones shown in Fig. 4, also serve as a way to determine stability thresholds for ITG or KBM modes. In order to evaluate these stability thresholds and their proximity to experimental conditions, the normalized ion temperature gradients, a/L_{T_i}, are increased at all minor radii shown in Table I. To summarize the results, only the dominant mode is identified for each condition. This is shown, for example, in Fig. 4(b) where a TEM mode is dominant at low $\beta_{e,unit}$ (or $\alpha_{MHD,unit}$) values, then an MTM mode is dominant near or at experimental conditions, and finally, a KBM mode that is triggered just above the experimental value becomes dominant.

The results for all the investigated radial positions are summarized in Fig. 6, which is a bar diagram showing all the dominant modes (largest growth rate) in the ion-scale range taking into account all the scans performed. The red lines are the experimental profiles for each parameter. In addition, the short horizontal green line indicates the KBM threshold. The KBM threshold is not always well defined; and in those cases, it is simply linearly extrapolated from the KBM unstable region. The short horizontal black line at some minor radius indicates when the dominant mode growth rate overcomes the $E \times B$ flow shear, γ_E. It can be observed that, even though MTMs are dominant under the experimental condition, KBM modes are at or near the threshold of being dominant. Since the dominant mode growth rates at $r/a = 0.6$ and 0.7 are already larger than γ_E, there is no γ_E–mark at those positions.

The high collisionality NSTX discharge analyzed in this section shows significant MTM activity at the experimental condition. The presence of MTMs in these regimes was investigated previously by Guttenfelder *et al.*,[22] and they are also well described by reduced models.[30] Their large growth rates are attributed to the sufficient high collisionality, plasma beta, and electron temperature gradient. However, it is interesting to note that other modes are present with, in some cases, similar growth rates as shown in Fig. 2 and that KBMs are right at the threshold of being dominant for at least two radial positions.

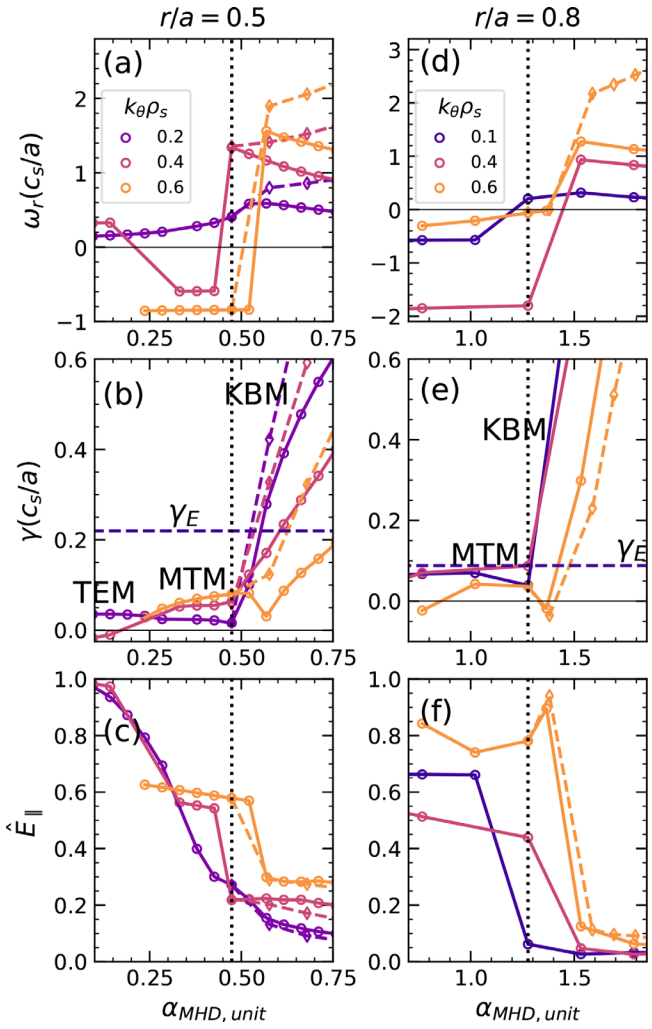

FIG. 4. High collisionality case: scans over plasma $\beta_{e,unit}$ (circle-solid curves) and ion temperature gradient, a/L_{T_i} (diamond-dashed curves) at radial positions $r/a = 0.5$ and 0.8. Three selected wavenumbers are shown at each case. Both scans are represented as the change in $\alpha_{MHD,unit}$ (see the Appendix). (a) and (d) show the real frequency, (b) and (e) the growth rate, and (c) and (f) the normalized electric field for each minor radius, respectively. The vertical dotted line indicates the experimental condition and the dashed horizontal line in (b) and (e) indicates the $E \times B$ flow shear growth rate, γ_E.

B. NSTX: Medium collisionality

The second discharge considered in this study is the medium collisionality NSTX discharge, whose kinetic profiles are presented in Fig. 1(b) and additional parameters at the radial position of interest are presented in Table I. As with the high collisionality case, Fig. 7 shows (a) the real frequency and (b) the growth rate of modes, at different minor radii and as a function of the normalized wavenumber. For this discharge, the $\alpha_{MHD,unit}$ (or pressure gradient) value at $r/a = 0.5$ is negative, and therefore, no unstable modes are found. Similarly, at $r/a = 0.4$ and 0.6, pressure gradient is very small, leading to very stable conditions in which modes present near zero growth rates resulting in a challenging situation for the code to converge. On the other hand, at $r/a = 0.7$ and 0.8, modes have appreciable growth rates, exceeding in both cases γ_E.

At $r/a = 0.7$ there are, at least, two different trends separated by $k_\theta\rho_s \sim 0.8$. Larger wavenumbers correspond to MTMs modes. They have, for example, negative frequencies and the eigenfunctions (not shown here) have tearing parity. To identify the modes at $r/a = 0.7$ when $k_\theta\rho_s < 0.8$ as well as at $r/a = 0.8$, auxiliary scans, shown in Fig. 8, over the ion temperature gradient (diamond-dotted curves) and the effective electron plasma beta (circle-solid curves) are performed. For both radial positions, Fig. 8 shows the real frequency, growth rate and normalized electric field for selected wavenumbers, $k_\theta\rho_s$'s. These quantities are plotted against $\alpha_{MHD,unit}$ as a way to combine both effective electron plasma beta and ion temperature gradient scans in the same figure (as it was done in Fig. 4 for the high collisionality case). As a reminder, the local equilibrium was maintained fixed throughout these scans. At $r/a = 0.7$, the growth rate trend, Fig. 7(b), looks like that of ITG modes (growth rate peaks at $k_\theta\rho_s \sim 0.4$). However, for low wavenumbers (see $k_\theta\rho_s \sim 0.1$ for $r/a = 0.7$ in Fig. 8), the mode behaves as a KBM since both plasma beta and ion temperature gradient scans show essentially the same trend when represented as a change in $\alpha_{MHD,unit}$. It is possible, however, that this mode shows slightly hybrid features at the experimental condition since the normalized parallel electric field is still high when compared to values at increased $\beta_{e,unit}$ (or $\alpha_{MHD,unit}$). As the wavenumber increases, the modes become less sensitive to the ion temperature gradient. When $k_\theta\rho_s = 0.4$, it is clear that the mode growth rate is no longer sensitive to the temperature gradient, as can be observed in Fig. 8(b) and, therefore, not an ITG mode. In fact, the mode is slightly stabilized when the normalized ion temperature gradient is increased above the experimental condition, and only after increasing it about three times ($\alpha_{MHD,unit} \approx 1.25$), the mode shows a clear transition to a KBM, which is also reflected by a fall in $\hat{E}_\parallel$ and a jump in the real frequency. On the other hand, the trend as $\beta_{e,unit}$ is scaled up is different: the growth rate and real frequency of the mode gradually increases while the normalized electric field gradually falls. This trend is more consistent with a hybrid mode. It also shows a threshold in the $\beta_{e,unit}$ indicating that the mode is affected by full electromagnetic effects. The analysis of the eigenfunctions, presented in Fig. 9, shows a broad waveform on the perturbed electric potential for low $\beta_{e,unit}$ values, which is consistent with TEM modes, and it evolves to a more ballooning like form as $\beta_{e,unit}$ increases. Although not shown here, for larger wavenumbers, the growth rate stabilization with the ion temperature gradient is enhanced and the normalized parallel electric field becomes even higher at experimental conditions. Therefore, at $r/a = 0.7$ and under the experimental condition, these modes behave as more KBM for low wavenumbers, followed by hybrid TEM/KBM behavior at intermediate wavenumbers, and finally as more TEM-like modes for larger wavenumbers.

At $r/a = 0.8$, the scans shown in Figs. 8(d)–8(f) reveal a similar trend: as the $\beta_{e,unit}$ increases, all the growth rates gradually increase while the normalized parallel electric field decreases. They all ultimately become KBM modes. A difference here is that, when looking at the real frequencies, Fig. 8(d), the modes gradually move from the electron diamagnetic direction (negative real frequencies) to the ion diamagnetic direction (positive real frequencies) as $\beta_{e,unit}$ (or $\alpha_{MHD,unit}$) increases. It is interesting to note that it is almost under the experimental condition when all the modes in the ion-scale range

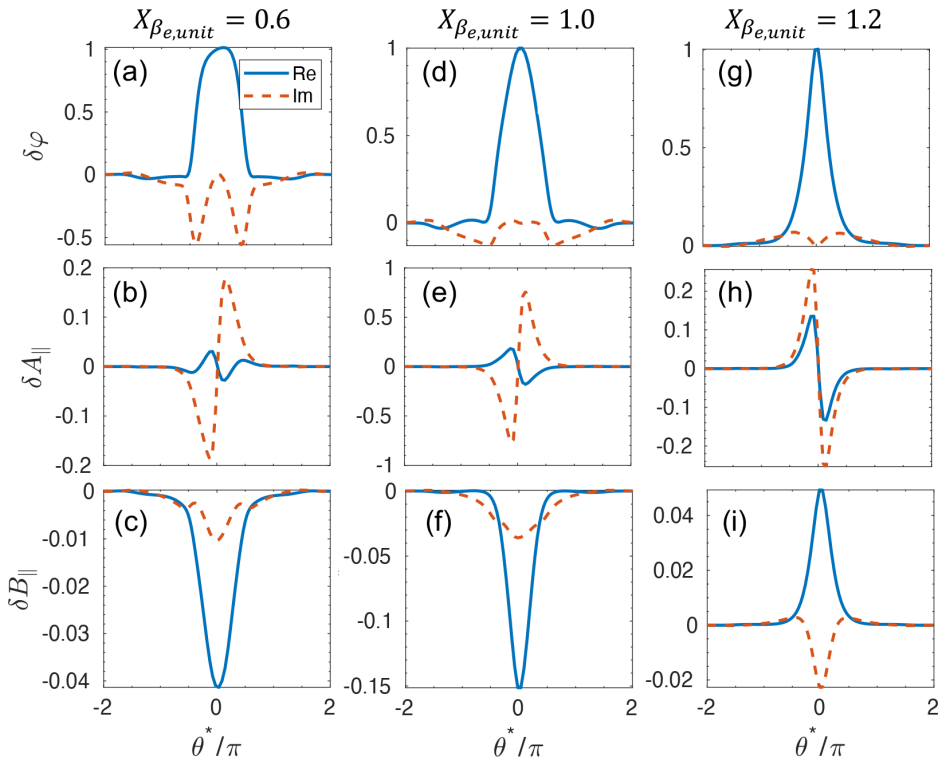

FIG. 5. High collisionality case: Eigenfunctions, $\delta\varphi$ (top), $\delta A_\parallel$ (middle), and $\delta B_\parallel$ (bottom), as a function of the ballooning angle for $k_\theta\rho_s = 0.6$, at $r/a = 0.8$, for different values of the $\beta_{e,unit}$ scaling factor, $X_{\beta_{e,unit}}$: 0.6 (a)–(c), 1.0 (d)–(f), and 1.2 (g)–(i). The experimental value is $\beta_{e,unit} = 0.59$, corresponding to $X_{\beta_{e,unit}} = 1.0$.

change from negative to positive values. At low beta values ($\alpha_{MHD,unit} \sim 0.75$), they all exhibit ballooning parity in their eigenfunctions, with broader perturbed electrostatic potential waveform and, as $\beta_{e,unit}$ is scaled up, their eigenfunctions resembles more those of a KBM mode, similar to Fig. 9 for $r/a = 0.7$.

Therefore, under the experimental condition, these modes also lie between TEM and KBM modes: for low wavenumbers ($k_\theta\rho_s \lesssim 0.1$), modes exhibit pure KBM characteristics. They have a very small normalized parallel electric field and their growth rates are very sensitive to increases in both $\beta_{e,unit}$ and a/L_{T_i} scaling factors. As the wavenumber increases, the mode growth rates become less sensitive to the ion temperature gradient, as occurred with the previous analysis at $r/a = 0.7$. Figures 8(d)–8(f) shows two cases, $k_\theta\rho_s = 0.6$ and 0.8, when the ion temperature gradient is increased. When $k_\theta\rho_s = 0.6$, the mode growth rate is slightly sensitive to the ion temperature gradient; and when $k_\theta\rho_s = 0.8$, the mode is actually stabilized. Following these behavior in a/L_{T_i} and $\beta_{e,unit}$, these modes are identified as Hybrid TEM/KBMs.

Although there are similarities between these hybrid modes at $r/a = 0.7$ and 0.8, they also exhibit differences. Figure 10 shows flux ratios and thermal diffusivity ratios for $k_\theta\rho_s = 0.4$ at $r/a = 0.7$ (a) and (b), and $k_\theta\rho_s = 0.6$ at $r/a = 0.8$ (c) and (d). Thermal diffusivities, χ_s, are defined through $Q_s = -n_s\chi_s dT_s/dr$ (where $s = e, i$ refers to electron and ion species), and for general definitions of how CGYRO calculates the fluxes, Q_s and Γ_s, see for example, Eqs. (35) and (36) in Ref. 31. The selected $k_\theta\rho_s$ are the wavenumbers with the largest growth rates under the experimental condition in each case. In both cases, the top panel shows electron and deuterium particle flux (Γ_e and Γ_D) as well as deuterium thermal flux (Q_D), normalized in all cases by the electron thermal flux (Q_e). The bottom panel shows deuterium (χ_D) and electron (χ_e) diffusivity ratios. It can be observed that, at $r/a = 0.7$, the ion thermal flux is comparable to the electron contribution. On the other hand, at $r/a = 0.8$, it is the electron flux that dominates over the ions. Therefore, these Hybrid TEM/KBM modes contribute to both ion and electron transport. At $r/a = 0.8$, both electron temperature and density gradients increase substantially, which may drive larger electron fluxes. The results in Fig. 10 suggest that this might also be related to whether the real frequency of the TEM that is coupled to the KBM is ion or electron directed, but further studies analysis are required. The results presented here are also in agreement with the observation that anomalous ion transport may arise at low collisionalities NSTX discharges in the outer plasma region.[9,11]

Additional scans are utilized to determine the ITG and KBM thresholds at other radii. Notably, at $r/a = 0.4$, normalized gradients determined from fits to the experimental profiles are relatively weak. As a consequence, no unstable modes are predicted for the nominal parameters. Figure 11(a) shows the growth rates at $r/a = 0.4$, as a function of the ion temperature gradient scaling factor, $X_{a/L_{T_i}}$, for three different wavenumbers, while (b) shows the growth rate as a function of $k_\theta\rho_s$ for three different $X_{a/L_{T_i}}$ values ($X_{a/L_{T_i}} = 1$ correspond to the experimental condition $a/L_{T_i} = 1.19$). It can observed that, after increasing $X_{a/L_{T_i}}$ twice the experimental value, ion temperature gradient dependent modes arise. These modes also present positive real frequency (in the ion diamagnetic direction). As shown in Fig. 11(b), the modes peak at $k_\theta\rho_s \sim 0.4$ consistent with ITG modes. In addition, the growth rate of different modes as a result of increasing $\beta_{e,unit}$ five times is included with a diamond–dashed curve. This increment leads to $\alpha_{MHD,unit} = 0.646$, which is almost twice the value

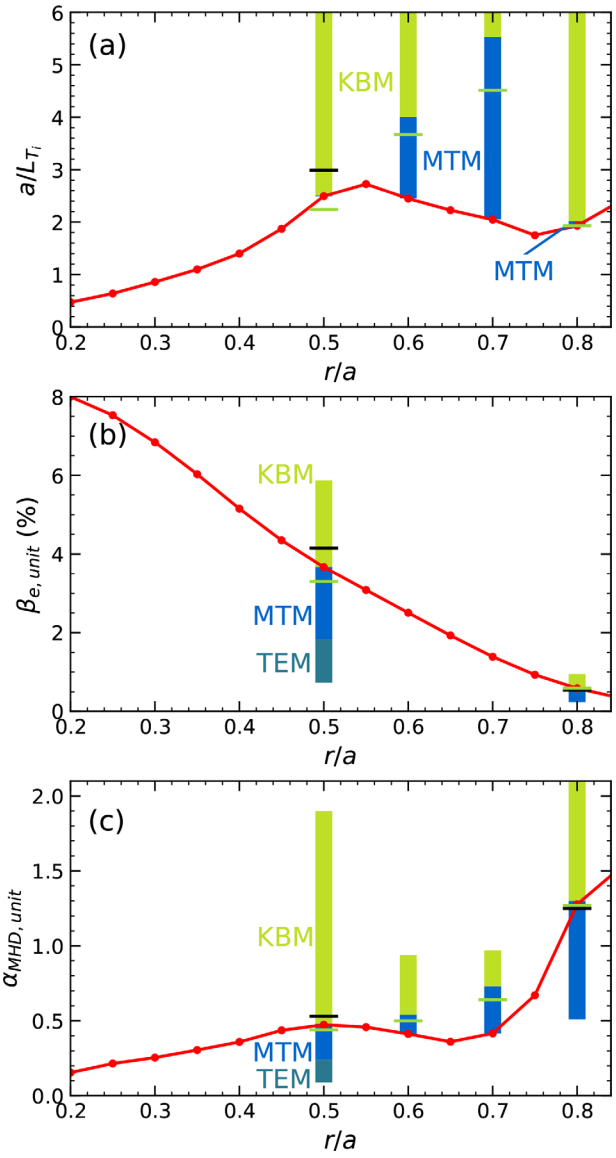

FIG. 6. High collisionality case: diagram of dominant modes in the ion-scale range when scaling (a) the normalized ion temperature gradient, a/L_{T_i}, and (b) the effective electron beta, $\beta_{e,unit}$. (c) Both scans can be represented and combined as the change in the $\alpha_{MHD,unit}$ parameter, since KBM modes are ultimately dependent on pressure gradient. The red line indicates the experimental profile, the short black lines indicate the condition in which the dominant mode overcomes the flow shear rate, γ_E, and the short green line indicates the KBM threshold.

obtained when $X_{a/L_{T_i}} = 3.5$. Only the modes around $k_\theta \rho_s \sim 0.05$ are recovered, consistent with KBMs, but the modes peaking around $k_\theta \rho_s \sim 0.4$ are only sensitive to ion temperature gradients, confirming that they are ITGs. In addition, Fig. 12 shows (a) flux ratios and (b) the thermal diffusivity ratio, χ_D/χ_e, for $k_\theta \rho = 0.4$, which also shows that deuterium fluxes dominate over electrons, in agreement with ITG modes.

As mentioned in Sec. I, even though ITG modes are often presented as electrostatic, they are affected by electromagnetic effects.

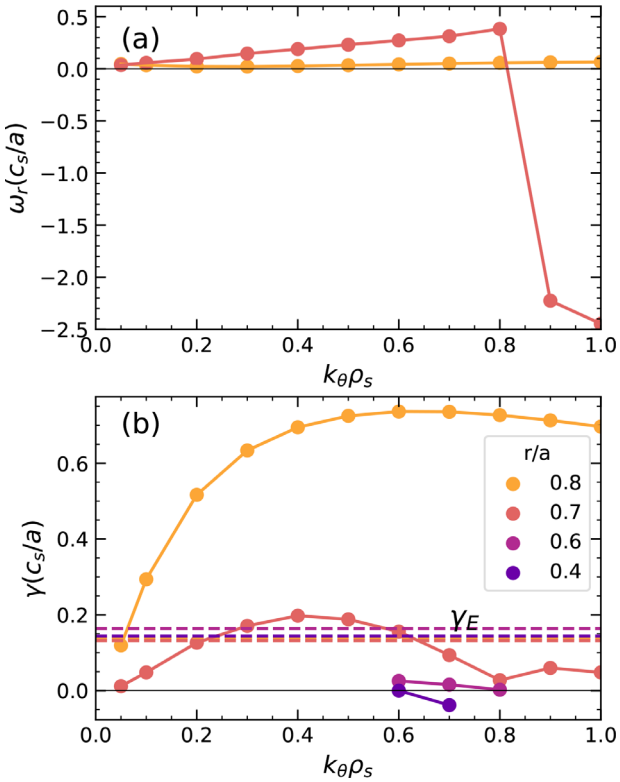

FIG. 7. Analysis of the medium collisionality discharge under experimental conditions. The figure shows (a) the real frequency, ω_n and (b) the growth rate, γ, both at different minor radii and as a function of the normalized wavenumber $k_\theta \rho_s$. The $E \times B$ flow shear growth rate, γ_E is included as a reference.

Figure 13 shows a comparison of the three different GK models implemented in CGYRO: the full electromagnetic model (that is being used throughout this study), an electromagnetic model with $\delta B_\parallel = 0$ (solving for $\delta\varphi$ and $\delta A_\parallel$), and the electrostatic model, which solves only for $\delta\varphi$ and has $\delta B_\parallel = \delta A_\parallel = 0$. The figure shows the $k_\theta \rho_s = 0.4$ ITG mode, presented before, as the normalized ion temperature gradient is scaled up. It is clear that full electromagnetic model (EM) effects are required to properly account for the growth rate, as they contribute to mode destabilization.[26,27] However, the mode's threshold can be well approximated by the $\delta B_\parallel = 0$ model, which has the benefit of excluding KBM modes. Therefore, even if they are not dominant in the full EM GK model, ITG modes could be found if they are subdominant, using the $\delta B_\parallel = 0$ GK model. Hence, simulations at other minor radii were conducted using this model, for the wavenumbers $k_\theta \rho_s = 0.3$, 0.4, as an approximation of the ITG threshold. At $r/a = 0.6$, a/L_{T_i} has to be increased over 2.4 times while at $r/a = 0.7$ and 0.8, no ITG modes were found even when increasing a/L_{T_i} over four times the experimental value.

To conclude this section, the bar diagram of dominant modes is presented in Fig. 14. It shows all the scans performed for this case. Again, the short horizontal black line, at some minor radii, indicates where the dominant mode overcomes the flow shear growth rate, γ_E, and the short horizontal green line indicates the KBM threshold. In addition, a short horizontal purple line in Fig. 14(a), at $r/a = 0.4$ and

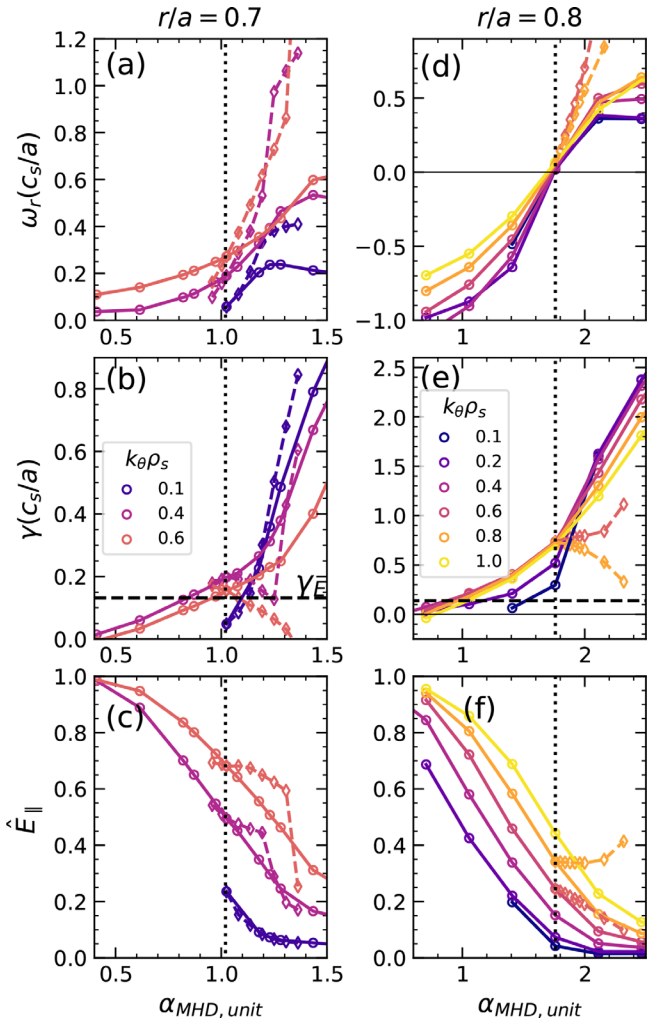

FIG. 8. Medium collisionality case: scans over plasma $\beta_{e,unit}$ (circle-solid curves) and ion temperature gradient, a/L_{T_i} (diamond-dashed curves), at radial positions $r/a = 0.7$ and 0.8. Both scans are represented as the change in $\alpha_{MHD,unit}$ (see the Appendix). For each radial position, (a) and (d) real frequency, (b) and (e) growth rate, and (c) and (f) normalized electric field are shown for selected wavenumbers, $k_\theta\rho_s$. The experimental condition is indicated with a vertical dotted line, and the $E \times B$ flow shear growth rate is included with a horizontal dashed line for reference.

0.6, indicates the ITG threshold, calculated with the $\delta B_\parallel = 0$ GK model in order to include subdominant cases as occurs at $r/a = 0.6$. No purple lines are at $r/a = 0.7$ and 0.8 since, as mentioned earlier, no ITG modes were found even when increasing a/L_{T_i} four times the experimental value. ITGs were found to be dominant only at $r/a = 0.4$ but only after increasing the normalized ion temperature gradient by a factor of ~2.3 above the experimental value. Although MTMs are present at some conditions, they were not found to be dominant at any condition. At $r/a = 0.7$ and 0.8, Hybrid TEM/KBM are dominant under experimental conditions with growth rates larger than γ_E, and with KBM overcoming them with small increases in either the temperature gradient or the plasma beta. In addition, Fig.14(c) shows the combination of both a/L_{T_i} and $\beta_{e,unit}$ scans into the $\alpha_{MHD,unit}$ parameter. However, the ITG bar is not shown here since, as contrary to KBMs, ITGs only depend on the ion temperature gradient. It can be observed that KBM thresholds are at or near the experimental $\alpha_{MHD,unit}$ value.

C. NSTX: Low collisionality

The third NSTX discharge considered in this study is the low collisionality discharge. The kinetic profiles and additional relevant parameters are presented in Fig. 1(c) and Table I, respectively. The results of the linear scan under experimental conditions are shown in Fig. 15. The first thing to note is that only at $r/a = 0.8$, the growth rate of several wavenumbers overcome the flow shear rate γ_E. At the other minor radii, all the modes exhibit growth rates well below γ_E. In addition, the real frequency shows linear dependency near the electron diamagnetic frequency, $\omega_r \sim \omega_{*e}$, at all the minor radii investigated for at least for some wavenumbers. Their eigenfunctions also have tearing parity, indicating the presence of MTMs. Between $r/a = 0.5$–0.7, they have much lower growth rates compared with the high collisionality case due to the reduced local values of electron beta, normalized electron temperature gradient and collisionality, all of which tend to weaken MTMs, as shown in Ref. 22 and 30. At $r/a = 0.8$, MTM growth rates are larger than in the high collisionality case due to the local increase in electron plasma beta and normalized electron temperature gradient associated with the broader temperature profiles observed in lower collisionality discharges.[11] On the other hand, since the overall $\alpha_{MHD,unit}$ is similar with the high collisionality discharge, KBMs are also found near the threshold. In addition to MTMs, other modes are present in this parameter region: Hybrid TEM/KBM modes at $r/a = 0.8$ for $0.1 < k_\theta\rho_s < 0.4$ and TEM modes at $r/a = 0.7$ for $k_\theta\rho_s > 0.4$. No unstable ITG modes were identified at the experimental conditions for any radii.

As done before, additional scans are used to identify ITG thresholds where possible. Again, only at $r/a = 0.4$ are dominant ITG modes found. The results are very similar to the medium collisionality case, shown in Fig. 11 and the ITG modes appears when $X_{a/L_{T_i}} > 3$. In addition, a comparison of the three different gyrokinetic models was also conducted for this case with similar findings as in the medium collisionality case, shown in Fig. 13.

The onset of KBM is found when increasing ion temperature gradient at the other minor radii, preventing the determination of any ITG threshold, if present, since only the dominant mode is determined in CGYRO. Auxiliary scans over the ion temperature gradient were conducted for wavenumbers $k_\theta\rho_s = 0.3, 0.4$, using the $\delta B_\parallel = 0$ GK model in order to estimate any possible ITG threshold. The results of all the scans are summarized in Fig. 16, which is a diagram of dominant modes for the low collisionality discharge. Figure 16(a) shows the scans over the ion temperature gradient and (b) the same scan but as the change in $\alpha_{MHD,unit}$. As in the previous cases, the short horizontal green line at all different minor radii indicates the KBM threshold and the short black line at some positions indicates when the dominant mode overcomes the flow shear rate. As it was mentioned before, only at $r/a = 0.8$, there are modes with growth rates larger than γ_E and therefore, no black line is indicated in that radial position. Figure 16(a) also shows a short horizontal purple line at almost all radial positions, indicating the estimation of the ITG threshold. There is no purple line at $r/a = 0.8$, since no ITG modes were found after increasing a/L_{T_i}

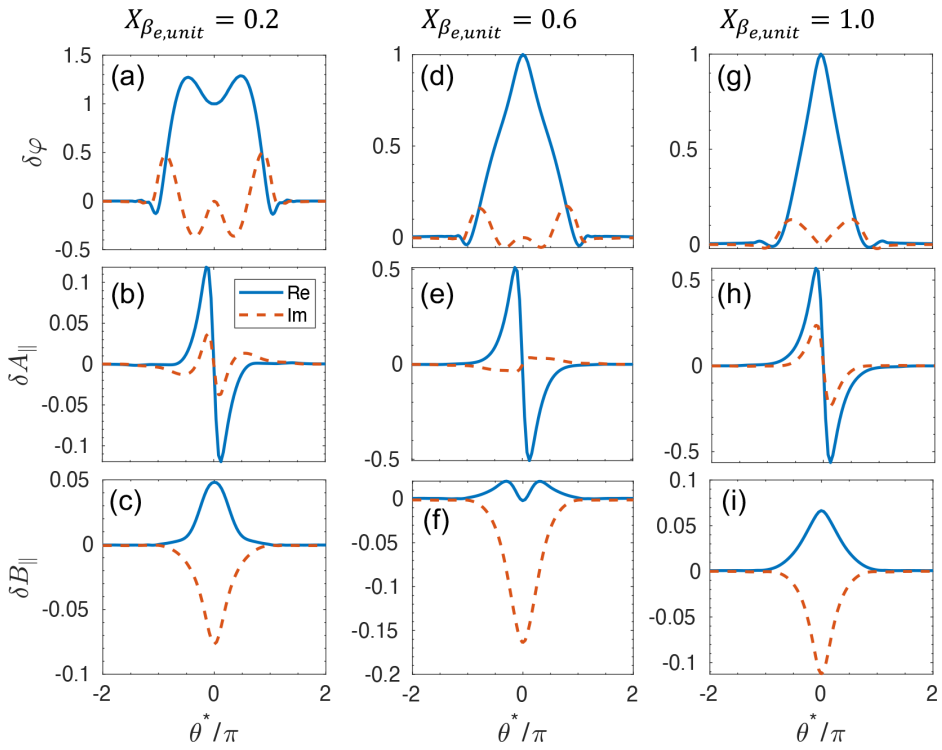

FIG. 9. Medium collisionality case: Eigenfunctions, $\delta\varphi$ (top), $\delta A_{\parallel}$ (middle), and $\delta B_{\parallel}$ (bottom), as a function of the ballooning angle for $k_\theta \rho_s = 0.4$, at $r/a = 0.7$, and for different values of the $\beta_{e,unit}$ scaling factor, $X_{\beta_{e,unit}}$: 0.2 (a)–(c), 0.6 (d)–(f), and 1.0 (g)–(i). The experimental value is $\beta_{e,unit} = 1.7$, corresponding to $X_{\beta_{e,unit}} = 1.0$.

more than four times, even with the $\delta B_{\parallel} = 0$ GK model. It is interesting to note that for all the cases where ITGs were found, KBMs are triggered first as the temperature gradient increases and they basically dominate over ITGs. The KBM thresholds are also near the experimental conditions at several radial positions, as can be noted in Fig. 16(b).

D. Summary of microstability in NSTX discharges

Extending previously published analyses, linear gyrokinetic simulations of these three NSTX discharges has shown a wide variety and complexity of modes. There are some general trends that appear across these cases. First, ITG modes are never predicted to be unstable for the experimental conditions. Only limited cases ($r/a = 0.4$ in medium and low collisionality discharges) were ITG modes dominant, and basically at all cases, with the exception of $r/a = 0.4$ in the medium collisionality discharge, their thresholds occur after those of the KBMs. Even though they were already introduced in the different diagrams, a summary of ITG thresholds in the medium and low collisionality discharge is given in Table II. The table shows, at the different radial positions investigated, the experimental ion temperature gradient R/L_{T_i}, the inferred threshold from the GK simulations, $(R/L_{T_i})^{(GK)}_{ITG}$ (using the $\delta B_{\parallel} = 0$ model and only for wavenumbers $k_\theta \rho_s = 0.3$ and 0.4), the simple ITG threshold formula[32] given by $(R/L_{T_i})^{(R)}_{ITG} = (4/3)(1 + T_i/T_e)$, and the expression given by Jenko *et al.*,[33] $(R/L_{T_i})^{(J)}_{ITG} = \max\{(1 + T_i/T_e)(1.33 + 1.91s/q)(1 - 1.5r/R)(1 + 0.3rd\kappa/dr,\ 0.8R/L_{n_i}\}$. The $*$ in the last column indicates that the threshold was determined by the density gradient in the above formula. It is worth noting that the two ITG threshold formulas were not intended for highly shaped, low aspect ratio tokamaks like NSTX, and the resulting discrepancy can be noticeable in the outer plasma region.

The absence of unstable ITG modes combined with the prediction that at many radial positions the remaining unstable modes have growth rates below the $E \times B$ flow shearing rate is consistent with the observation that NSTX H-mode discharges have ion transport close to the neoclassical level. At many radii, the experimental profiles are predicted to be close to or just beyond the KBM threshold, which suggests they might also play a role limiting the confinement. However, it remains to be understood how KBMs can contribute to multi-channel transport in a way that is consistent with NSTX experimental observations, which show predominantly anomalous electron thermal transport while ion thermal transport is observed to be mostly neoclassical.

III. NSTX-U PROJECTION

The findings in Sec. II suggested the absence of unstable ITG modes in high-β NSTX H-modes. However, it is unknown whether they may become more important for higher temperature, lower collisionality discharges expected in NSTX-U. To explore this situation, an NSTX-U projection which is part of different scenario projections reported at Ref. 34 was analyzed. These projections were explored using TRANSP and, in this work, the run 121123*K*55 was selected. This run is based on an NSTX discharge in which experimental profile shapes for the electron density and temperature were employed, and the density was scaled to reach a different Greenwald fraction, f_{GW}. The ion thermal transport was assumed to be neoclassical, and the electron temperature was adjusted to match energy confinement time scalings. The resulting projected temperatures are higher than those of the NSTX discharges studied due to the increased field strength and

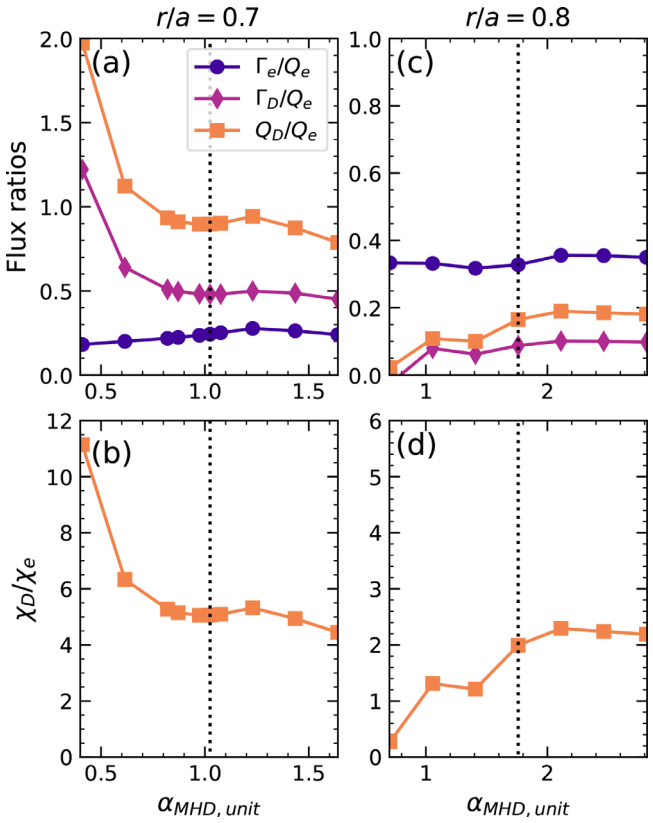

FIG. 10. Medium collisionality case: flux ratios (top) and thermal diffusivity ratio (bottom) at $r/a = 0.7$ (left) and 0.8 (right), for the dominant mode under the experimental condition ($k_\theta \rho_s = 0.4$ and 0.6, respectively). In both cases, the $\beta_{e,unit}$ scan is represented as a change in the $\alpha_{MHD,unit}$ parameter. At $r/a = 0.7$, the Hybrid TEM/KBM mode has a significant ion contribution to the flux, whereas at $r/a = 0.8$, the electron contribution dominates.

heating power. Additionally, outside $r/a > 0.6$ the normalized ion temperature gradients are projected to be much higher than in the NSTX cases and, therefore, likely represent a good case to test whether ITG modes are ever predicted to be unstable.

Figure 17 shows the kinetic profiles at two different times: 11.8 and 14.5 s in the TRANSP simulation, corresponding to $f_{GW} = 0.7$ and 0.55, respectively. The former time was used in Ref. 34 but the latter provides even higher temperatures and temperature gradients making it a better candidate to investigate ion temperature gradient driven modes. Additional information is summarized in Table III for the two selected times. It can be clearly noted that the collisionalities are much lower than in the previous NSTX cases.

Real frequencies and growth rates as a function of the normalized wavenumber, $k_\theta \rho_s$, are shown in Fig. 18 for different minor radii. The figure shows the results for three different cases at 11 800 ms (a) and (b), at 14 500 ms (c) and (d), and at 14 500 ms but turning off $\delta B_\parallel$ (e) and (f). At first glance, mode activity looks much stronger than the previously analyzed NSTX cases: all the minor radii investigated present modes with growth rates larger than the flow shear rate. Since the zoology of modes is very similar between the cases (a) and (b) (at

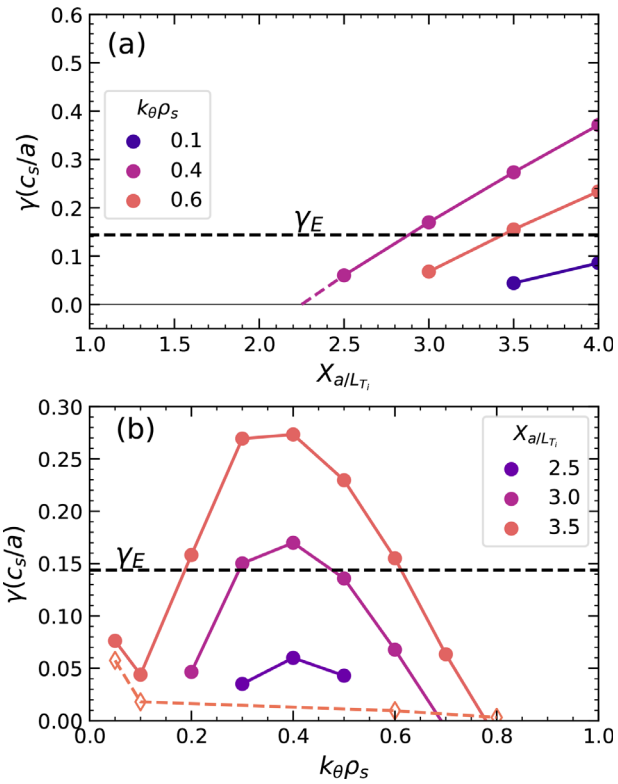

FIG. 11. Medium collisionality case: growth rates at $r/a = 0.4$ when (a) increasing the normalized ion temperature gradient scaling factor, $X_{a/L_{T_i}}$ and (b) as a function of wavenumber for three different $X_{a/L_{T_i}}$ values. When $X_{a/L_{T_i}} > 2.2$ approximately, an ITG mode is triggered. In (b), the diamond-dashed line was obtained increasing only $\beta_{e,unit}$ five times, showing that the mode is not pressure sensitive.

11 800 ms) and (c) and (d) (at 14 500 ms), only the case latter will be analyzed in the following.

To identify all the modes present, it can be noted first that at $r/a = 0.7$ and 0.8, there are modes whose real frequency, as shown in

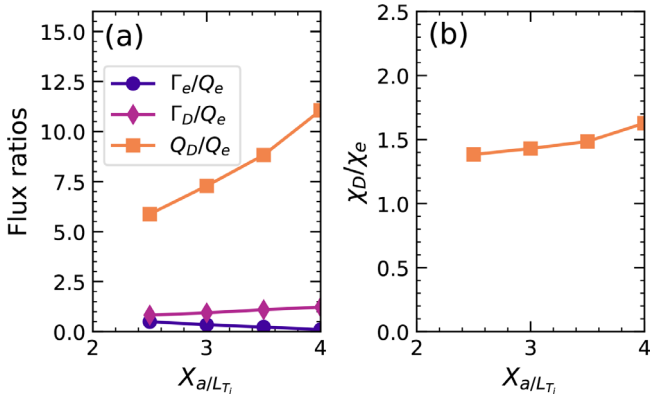

FIG. 12. Medium collisionality case: (a) flux ratios and (b) thermal diffusivity ratio at $r/a = 0.4$ for the $k_\theta \rho_s = 0.4$ ITG mode, showing a large deuterium over electron contribution to the thermal flux.

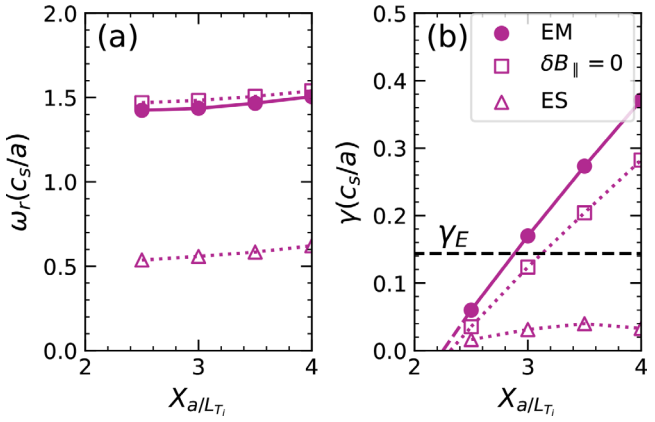

FIG. 13. Medium collisionality case: (a) real frequency and (b) growth rate for the $k_\theta\rho_s = 0.4$ ITG mode at $r/a = 0.4$. The figure shows a comparison of the full electromagnetic model (EM), the electromagnetic model with $\delta B_\parallel = 0$, and the electrostatic model (ES), which has $\delta B_\parallel = \delta A_\parallel = 0$.

Fig. 18(c), agrees with ω_{*e}, exhibit tearing parity, and are unaffected by turning off $\delta B_\parallel$ [see Fig. 18(e)], in agreement with MTM modes. For all the other modes present, scans varying the ion temperature gradient scale length and plasma beta were conducted for the entire ion scale range, as with the NSTX cases.

At $r/a = 0.4$, the modes were identified as KBM, having positive frequencies, ballooning parity eigenfunctions, very low $\hat{E}_\parallel$ value and being very sensitive to both a/L_{T_i} and $\beta_{e,unit}$. The same modes are present at $r/a = 0.5$, 0.6 and 0.7 at low wavenumbers. Figure 18(c) also shows $\omega_p/2 = [k_\theta\rho_s(a/L_{T_i} + a/L_{n_i}) + k_\theta\rho_s(a/L_{T_e} + a/L_{n_e})]/2$, with dotted lines, for $r/a = 0.4, 0.5$, and 0.6. There is a clear agreement between ω_r and $\omega_p/2$ at low $k_\theta\rho_s$. In addition, growth rate spectra peak as $k_\theta\rho_s \to 0$. These features agree with the fact that the modes are KBMs and they were investigated in detail in Ref. 35. Figure 19 shows scans over a/L_{T_i} and $\beta_{e,unit}$ at selected wavenumbers and at three different minor radius. For each minor radius, the figure shows the real frequency, the growth rate, and the normalized parallel electric field. It can be observed that, at $r/a = 0.5$ [see Figs. 19(a)–19(c)], the growth rate of the $k_\theta\rho_s = 0.05$ mode is, indeed, very sensitive to both a/L_{T_i} and $\beta_{e,unit}$ while having a very low $\hat{E}_\parallel$ value, corresponding to a KBM mode. In addition to these KBM modes at low wavenumbers, there are ballooning parity modes at $k_\theta\rho_s > 0.2$ in Fig. 18(d) with the real frequency around zero. Figure 19(b) shows that the growth rate of $k_\theta\rho_s = 0.4$ and 0.7 are not sensitive, in the vicinity of the experimental value, to the ion temperature gradient and that for $k_\theta\rho_s = 0.7$, the mode is actually stabilized when a/L_{T_i} is increased and are likely TEM modes. In addition, at $k_\theta\rho_s = 0.4$, the mode is near the KBM threshold, which is characterized by the sudden drop in $\hat{E}_\parallel$ and the increase in the real frequency as well as a stronger sensitivity to $\alpha_{MHD,unit}$.

At $r/a = 0.8$, in addition to the MTM modes described before, there are also two modes, with $k_\theta\rho_s = 0.2$ and 0.3, that have positive real frequencies [see Fig. 18(d)]. In fact, these modes have very similar growth rate to the MTM modes that are obtained when turning $\delta B_\parallel$ off for the same wavenumbers, as can be noted when comparing Figs. 18(e) and 18(f). These two types of modes are basically coexisting with similar growth rates. Scans shown in Figs. 19(d)–19(f) show that, for $k_\theta\rho_s = 0.2$ and for small values of $\alpha_{MHD,unit}$, the growth rate is

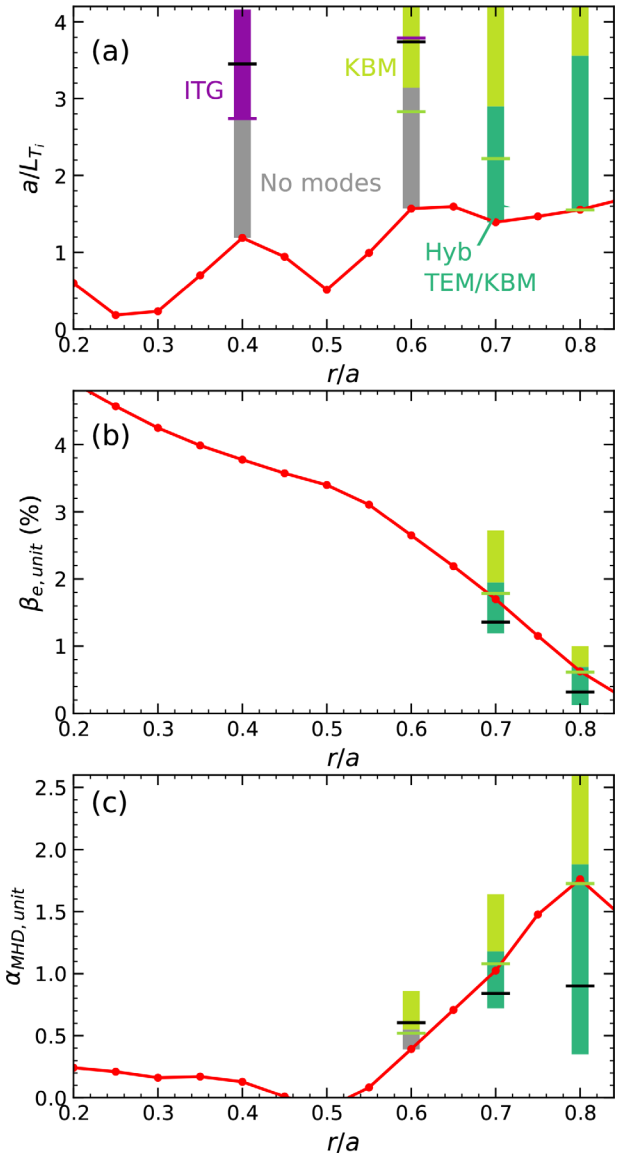

FIG. 14. Medium collisionality case: diagram of dominant modes in the ion-scale range when scaling (a) the normalized ion temperature gradient, a/L_{T_i}, and (b) the effective electron plasma beta, $\beta_{e,unit}$. (c) Both scans are combined and represented as the change in the $\alpha_{MHD,unit}$ parameter, except for $r/a = 0.4$, since KBM modes are ultimately dependent on pressure gradient. The red line indicates the experimental profile, and the short black line at some radial position indicates the condition in which the dominant mode overcomes the flow shear rate, γ_E. The short green and purple lines indicate the KBM and ITG threshold, respectively (ITGs are shown only in the a/L_{T_i} scan).

essentially independent of the both a/L_{T_i} and $\beta_{e,unit}$. The modes have positive real frequency, present ballooning parity (not shown here) and large $\hat{E}_\parallel$ value. Therefore, under this condition, this mode behaves as a TEM. As $\alpha_{MHD,unit}$ reaches the experimental condition, the mode is at the threshold of the transition to a KBM (given by the growth rate sensitivity on $\alpha_{MHD,unit}$, the low normalized parallel electric field and

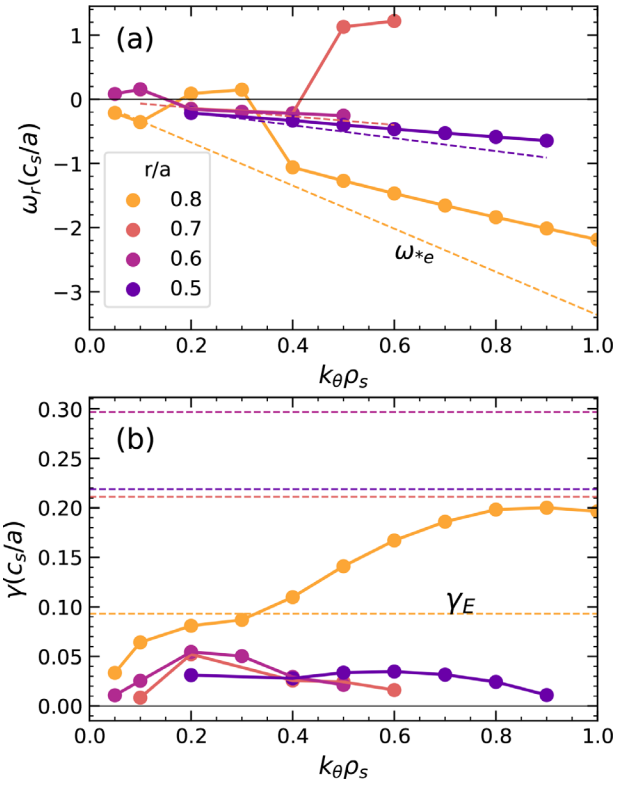

FIG. 15. Analysis of the low collisionality discharge under the experimental condition. (a) shows the real frequency, ω_r, and (b) shows the growth rate, γ, both at different minor radius and as a function of the normalized wavenumber $k_\theta\rho_s$. The electron diamagnetic drift frequency, ω_{*e}, and the $E\times B$ flow shear growth rate, γ_E, are included as a reference.

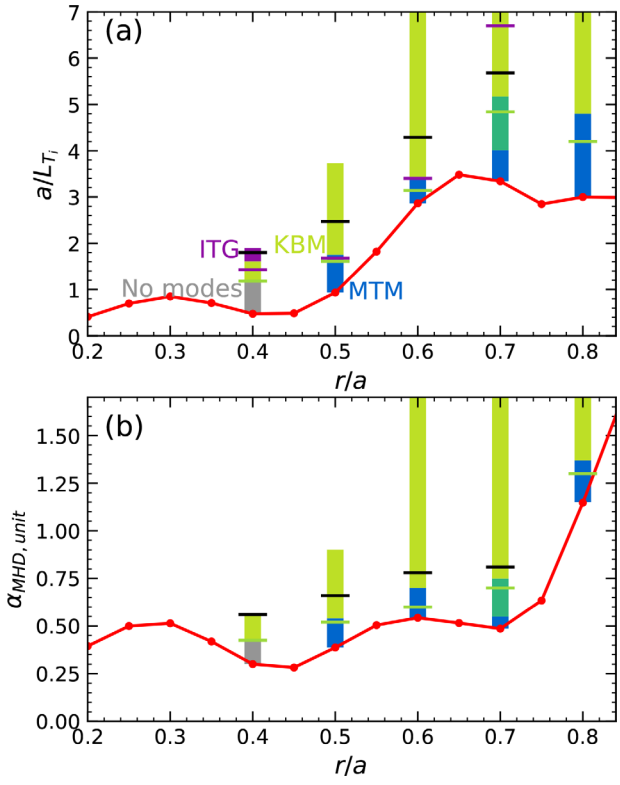

FIG. 16. Low collisionality case: diagram of dominant modes in the ion-scale range when varying (a) the ion temperature gradient scale length. In (b), the diagram is represented as the change in the $\alpha_{MHD,unit}$ parameter. The red line indicates the experimental profile, and the short black line at the some radial position indicates the condition in which the dominant mode overcomes the flow shear rate, γ_E. The short green and purple lines indicate KBM and ITG thresholds, respectively.

positive real frequency), but the normalized parallel electric field is still decreasing and the growth rate did not start increasing yet, therefore behaving as a Hybrid TEM/KBM. Finally, when $\alpha_{MHD,unit}$ increases over the experimental value, the normalized parallel electric field falls to a very low values and the mode behaves as a pure KBM. For completeness, the $k_\theta\rho_s = 0.4$ shows an example of the fact that the previously described MTMs transition also to KBMs: the modes have negative real frequency for small $\alpha_{MHD,unit}$ values and tearing parity (not shown here). They are insensitive to a/L_{T_i} scans as well as to $\beta_{e,unit}$, for the range considered. As $\alpha_{MHD,unit}$ increases, the real frequency jumps to a positive values, while the normalized electric field falls to small values, and the growth rate becomes sensitive to both $\beta_{e,unit}$ and a/L_{T_i} scans. This behavior is similar to that described in Fig. 4.

At $r/a = 0.9$, there are also two distinct trends of modes that are separated by $k_\theta\rho_s \sim 0.8$ [see Figs. 18(c) and 18(d)]. Modes with $k_\theta\rho_s < 0.8$ show the positive frequency. In particular, the $k_\theta\rho_s = 0.05$ presents ballooning parity (not shown here) and, as shown in Figs. 19(g)–19(i), the mode is at the KBM threshold. Larger wavenumbers, for example $k_\theta\rho_s = 0.3$, which is at the peak in the growth rate trend at the experimental condition, shows ballooning parity but a larger $\hat{E}_\parallel$ value and the slow transition that can be observed in this case, as $\alpha_{MHD,unit}$ [Figs. 19(g)–19(i)], suggest that these modes are hybrid TEM/KBMs. In addition, turning $\delta B_\parallel$ off wipes out these modes, as shown in Figs. 18(e) and 18(f), and MTMs with slightly smaller growth rates are revealed. On the other hand, modes with $k_\theta\rho_s > 0.8$ have negative frequency and

TABLE II. ITG thresholds in the medium and low collisionality NSTX discharges.

r/a	$R/L_{T_i}^{(\exp)}$	$(R/L_{T_i})_{ITG}^{(GK)}$	$(R/L_{T_i})_{ITG}^{(R)}$	$(R/L_{T_i})_{ITG}^{(J)}$
		(a) Medium collisionality discharge		
0.4	1.85	4.2	2.59	2.16
0.6	2.37	5.7	2.52	2.18
0.7	2.07	> 8.3	2.53	6.16*
0.8	2.25	> 9.0	2.74	7.78*
		(b) Low collisionality discharge		
0.4	0.79	2.4	2.94	2.58
0.5	1.53	2.7	2.96	2.26
0.6	4.59	5.5	2.86	1.87
0.7	5.22	10.4	2.64	1.34
0.8	4.55	> 18	2.58	1.18*

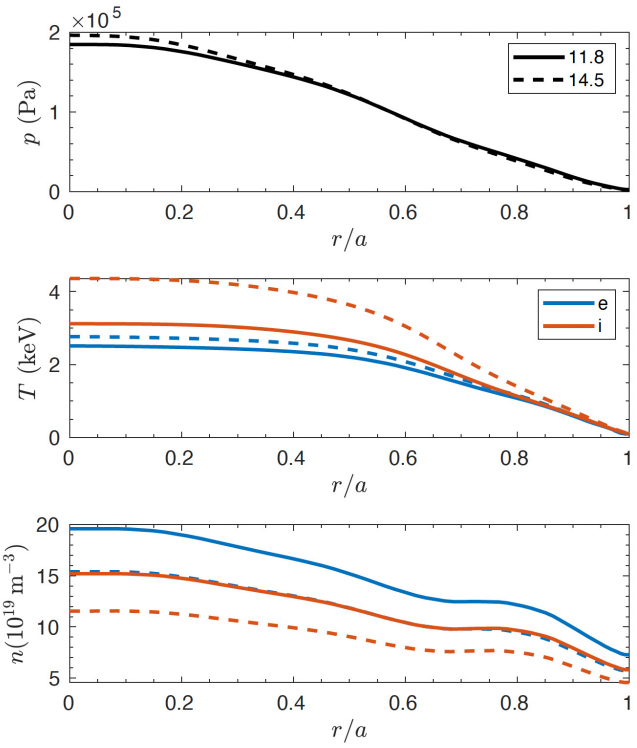

FIG. 17. Kinetic profiles of the NSTX-U projection (TRANSP run 121123*K*55) at two different times: 11 800 and 14 500 ms. The Greenwald limit was set to 0.7 and 0.55, respectively.

they are essentially unaffected when turning $\delta B_{\parallel}$ off. They are also insensitive to changes in either the ion temperature gradient or plasma beta, as shown in Figs. 19(g)–19(i). However, their negative real frequencies are not in agreement with the electron diamagnetic frequency and an example of their eigenfunctions is shown in Fig. 20. Additional scans reveal these modes have a clear threshold in electron temperature gradient. Opposite to TEM expectations, the modes are also stabilized completely by increasing density gradient. Taken together, these modes are identified to be electron-scale ETG instabilities, at the long-wavelength limit of a much broader wavenumber range of unstable modes. While ETG instabilities predicted in the core tend to occur at much higher wavenumbers ($k_\theta \rho_s > 2$–3), the relatively large normalized gradients associated with the edge/pedestal region have been shown to drive unstable ETG at lower wavenumbers approaching ion scales.[36,37] Interestingly, the inferred threshold for instability derived from the electron temperature and density gradient scans is found to be $\eta_{e,crit} \approx 1.7$ for the ETG modes here, very similar to that found in pedestal studies on NSTX[38,39] and DIII-D.[40] Therefore, in this projection, KBM, MTM, Hybrid TEM/KBM, and ETG modes are found unstable at ion-scale wavelengths with growth rates exceeding the flow shear rate. It is important to note here that, even though ETG were found present in the long wavelength limit, the analysis of those modes remains out of scope of the present study.

It is worth noting that ITG modes are not found to be unstable even at the very low collisionality and large temperature gradients presented in this projection. To explore whether ITG thresholds are near the projection condition, scans increasing the ion temperature gradient were conducted at all the different minor radii without evidence of ITG being present when using the full EM model in CGYRO. When employing the $\delta B_{\parallel} = 0$ model, subdominant ITG modes are found at $r/a = 0.4$–0.6 when increasing the ion temperature gradient over the projected value. This is summarized in Table IV, which is similar to Table II presented for previous NSTX cases. At $r/a = 0.5$ and 0.6, the estimated threshold is close to the projected value, but in those cases, KBMs are already unstable and they might prevent ITG from ever being triggered. In addition, similarly to the NSTX cases, ITG thresholds become very large in the outer region ($r/a \gtrsim 0.7$), largely

TABLE III. Summary of relevant data at different minor radii for the NSTX-U projection (TRANSP ID 121123*K*55).

R/a	κ	δ	q	s	$\beta_{e,unit}$ (%)	T_i/T_e	a/L_{T_e}	a/L_{n_e}	a/L_{T_i}	a/L_{n_i}	$\alpha_{MHD,unit}$	Z_{eff}	$\nu^{e/i}$	γ_E (c_s/a)
(a) At 11 800 ms with a Greenwald limit of 0.7														
0.4	2.20	0.120	1.47	0.555	3.89	1.22	0.427	0.730	0.592	0.730	0.408	2.0	0.274	0.032 6
0.5	2.24	0.145	1.66	0.530	2.94	1.21	0.928	1.15	1.10	1.15	0.677	2.0	0.284	0.058 4
0.6	2.26	0.164	1.88	0.978	2.01	1.18	1.98	1.23	2.22	1.23	0.885	2.0	0.330	0.091 2
0.7	2.28	0.187	2.38	2.24	1.17	1.13	2.96	−0.0150	3.58	−0.0150	0.775	2.0	0.500	0.069 6
0.8	2.34	0.228	3.43	3.16	0.576	1.05	3.68	0.922	4.48	0.922	1.14	2.0	0.914	0.014 6
0.9	2.45	0.294	5.26	4.42	0.170	1.05	9.42	3.23	8.62	3.23	1.90	2.0	2.36	−0.007 03
(b) At 14 500 ms with a Greenwald limit of 0.55														
0.4	2.06	0.096	1.23	0.502	3.68	1.53	0.454	0.750	0.661	0.750	0.325	2.0	0.178	0.048 3
0.5	2.10	0.114	1.39	0.588	2.80	1.50	0.972	1.17	1.20	1.17	0.529	2.0	0.186	0.085 8
0.6	2.12	0.131	1.59	1.05	1.88	1.46	2.04	1.22	2.45	1.22	0.695	2.0	0.219	0.129
0.7	2.15	0.149	2.03	2.17	1.09	1.36	3.04	−0.0446	3.99	−0.0446	0.623	2.0	0.339	0.098 4
0.8	2.22	0.179	2.87	3.05	0.544	1.21	3.82	0.973	5.02	0.973	0.883	2.0	0.621	0.018 3
0.9	2.33	0.227	4.37	4.33	0.156	1.18	9.98	3.27	9.22	3.27	1.340	2.0	1.68	−0.008 96

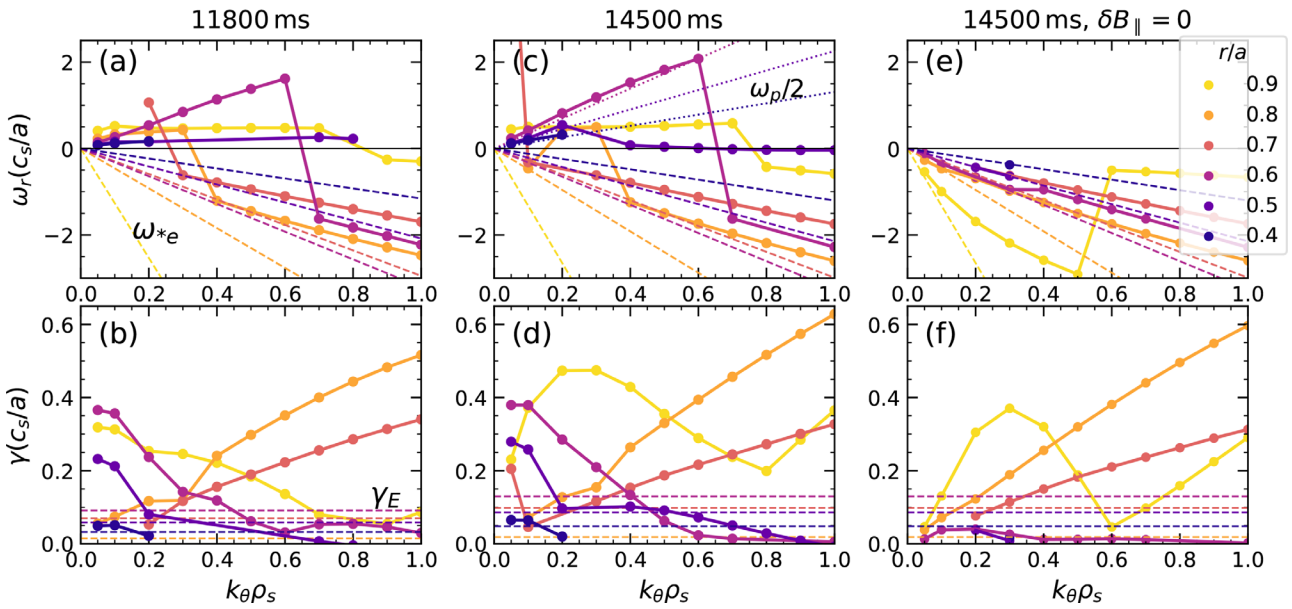

FIG. 18. Real frequency, ω_n and growth rate, γ, as a function of the normalized wavenumber, $k_\theta\rho_s$, at different minor radii for the NSTX-U projection 121123*K*55. (a) and (b) shows the results at 11 800 ms, (c) and (d) at 14 500 ms, and (e) and (f) shows the results at 14 500 ms but turning off $\delta B_\parallel$ in the gyrokinetic equation.

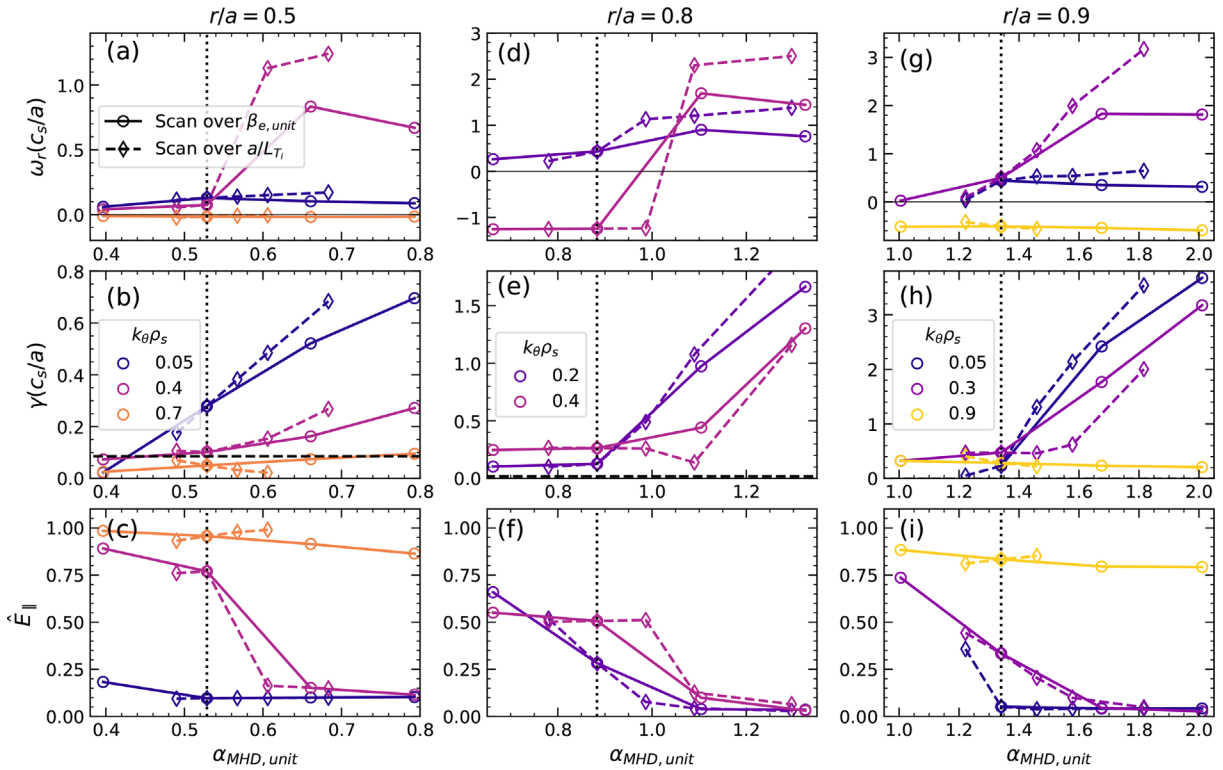

FIG. 19. NSTX-U projection: scans over ion temperature gradient, a/L_{T_i} (diamond-dashed curves), and plasma beta, $\beta_{e,unit}$ (circle-solid curves), for selected wavenumbers at three different radial positions: $r/a = 0.5$, 0.8, and 0.9. Scans are represented as the change in $\alpha_{MHD,unit}$ (see the Appendix). For each radial position, the figure shows the real frequency, the growth rate, and the normalized electric field of the modes. The vertical dotted line indicates the experimental condition, and the dashed horizontal line in the growth rate panels indicates the $E \times B$ flow shear rate, γ_E.

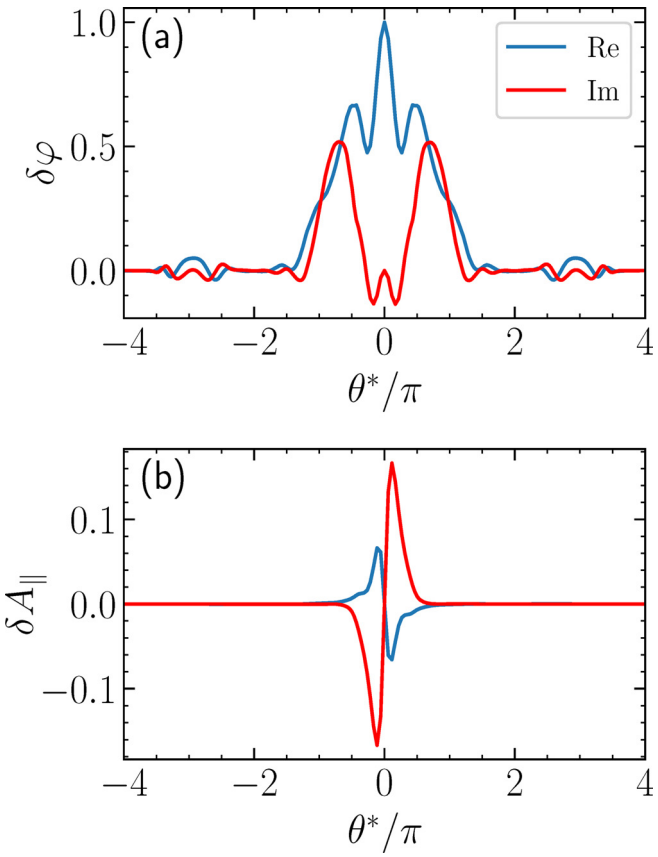

FIG. 20. NSTX-U projection: (a) perturbed electrostatic potential and (b) parallel component of the vector potential eigenfunctions, both as a function of the ballooning angle, corresponding to the $k_\theta \rho_s = 0.9$ and $r/a = 0.9$ case shown in Figs. 18(c) and 18(d).

exceeding the simple threshold values provided by $(R/L_{T_i})^{(R)}_{ITG}$ and $(R/L_{T_i})^{(J)}_{ITG}$.

Finally, a diagram of the dominant modes determined from various scans is summarized in Fig. 21. In this case, KBM modes are already present at the projection condition and they are also the dominant mode at some radial positions. Again, it is worth noting that KBM thresholds, given by the green short horizontal line, are close to the projection condition at several minor radii. The growth rates of the

TABLE IV. ITG thresholds in the NSTX-U projection at 14 500 ms.

r/a	$R/L_{T_i}^{(\exp)}$	$(R/L_{T_i})^{(GK)}_{ITG}$	$(R/L_{T_i})^{(R)}_{ITG}$	$(R/L_{T_i})^{(J)}_{ITG}$
0.4	1.28	3.1	3.37	3.84
0.5	2.29	2.75	3.33	3.42
0.6	4.62	5.56	3.28	3.47
0.7	7.40	>30	3.15	3.81
0.8	9.09	>36	2.95	3.04
0.9	16.3	> 65	2.91	4.61*

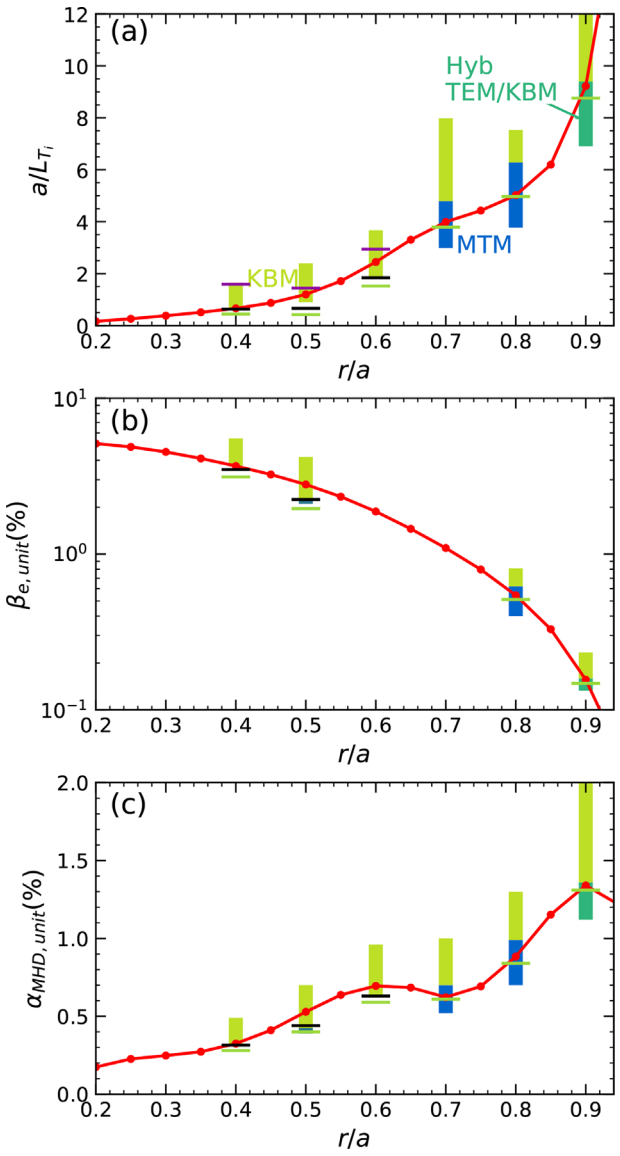

FIG. 21. NSTX-U projection 121123*K*55 at the 14 500 ms diagram of dominant modes in the ion-scale range when varying (a) the ion temperature gradient scale length and (b) the plasma $\beta_{e,unit}$ parameter. (c) shows a combination of both scans as a change in $\alpha_{MHD,unit}$. The red line indicates the experimental profile, the short black line at some radial positions indicates the condition in which the dominant mode overcomes the flow shear rate, γ_E. The short green and purple lines indicate KBM and ITG thresholds, respectively (ITG threshold is only shown for a/L_{T_i}).

dominant modes are larger than the flow shear rate, γ_E, at all the radial positions investigated, contrary to the NSTX results. MTM were also found to be present and dominant at two radial positions with large growth rates even the lower collisionality of the discharge. The presence of MTMs in these regimes could be attributed to very large electron temperature gradients or other factors, such as large $\beta_{e,unit}$, and they might be subject of future research. No unstable ITG modes were found throughout the scans performed for this NSTX-U projection

when using the full electromagnetic model, but they appear at some minor radii when turning $\delta B_{\parallel}$ off in the model, and after increasing the ion temperature gradient over the projected condition. This is indicated with the short horizontal purple line in Fig. 21(a). In all cases, KBM thresholds are lower that those of ITGs; and therefore, the transport may be limited by the former rather than the latter. The fact that KBM, TEM, and Hybrid TEM/KBM modes are unstable will probably deviate the ion transport from neoclassical assumptions to an anomalous behavior,[9,11] but this will require nonlinear simulations and might be also subject of future research.

IV. CONCLUSIONS

Comprehensive linear gyrokinetics scans for both NSTX discharges and NSTX-U projections were conducted in the ion-scale wavelength range to identify modes and thresholds in the region $r/a \sim 0.4$–0.9 for different collisionality regimes. This is the first time that a gyrokinetic analysis has been performed for a low collisionality NSTX-U projection and constitutes an important step toward the analysis of the anomalous transport that might occur in those regimes. The gyrokinetic code CGYRO was employed to conduct all the simulations. As noted in previous studies, a complex zoology of modes was found throughout all the cases. This work attempts to provide clarity on this by identifying relevant thresholds and dominance of the various instabilities.

An NSTX case with high collisionality was chosen as a starting point, followed by a medium and low collisionality regimes, and finally, by an NSTX-U projection with collisionality even lower than that of NSTX. While all input parameters vary from one discharge to the next, a number of general features and trends are apparent. In many cases throughout the different NSTX discharges, growth rates under the experimental condition were found to be smaller than the flow shear rate, in agreement with the fact that the neoclassical ion transport is usually found to dominate most of NSTX discharges. However, for lower collisionality regimes as well as in the NSTX-U projection, hybrid TEM/KBM modes arise with growth rates larger than the flow shear rate, at some radial positions, exhibiting in some cases significant ion-over-electron thermal flux. The NSTX-U projection also showed unstable KBM modes that could contribute to ion thermal transport but with thresholds close to the projected value.

In addition, general remarks about ITG and KBM thresholds can be made. First, ITGs were never predicted to be dominant at any radial position investigated in all the discharges. Second, when scanning over the ion temperature gradient, KBMs were found to be triggered almost always first than ITGs. Only in two cases were ITGs found to dominate after increasing the ion temperature gradient several times the experimental value. Third, additional ITG thresholds were identified by using the gyrokinetic model with $\delta B_{\parallel} = 0$ (suppressing KBM activity), but it was found that KBM thresholds (obtained with the full electromagnetic model) occur earlier than those of ITGs (with the exception of only one case). Fourth, KBM thresholds were found close to the experimental or projected value at almost all the radial positions investigated.

A summary of the ITG and KBM thresholds, combining the results of all the analyzed cases, is presented in Fig. 22. Figure 22(a) shows $(R/L_{T_i})^{(GK)}_{ITG}$ vs the experimental value $R/L^{(\exp)}_{T_i}$ for the same radial position and discharge, while Fig. 22(b) shows the KBM threshold, $\alpha^{(KBM)}_{MHD,unit}$ vs the experimental value $\alpha^{(\exp)}_{MHD,unit}$. The dashed line in both figures represents the condition $y = x$. As mentioned before, ITG thresholds were determined with the $\delta B_{\parallel} = 0$ gyrokinetic model. Since at some cases ITG thresholds were not found even after increasing the ion temperature gradient four times, open symbols were used in Fig. 22(a) and a thin dashed line ($y = 4x$) is also indicated for reference. These open symbols are, therefore, not thresholds but indicate that actual thresholds are at even higher gradients.

It is clear from this figure that ITG instability thresholds are typically much higher than experimental ion temperature gradients in high-beta NSTX H-mode plasmas. They are also generally higher than the gradients in the low collisionality NSTX-U scenario. We remind the reader that this scenario was a projection assuming that the ion temperature is limited only by neoclassical transport, indicating that ITG instabilities may not be expected to contribute to thermal losses in high performance NSTX-U discharges. As discussed in the Introduction, this result is expected (even when ignoring flow shear stabilization effects) due to multiple stabilizing effects that occur in

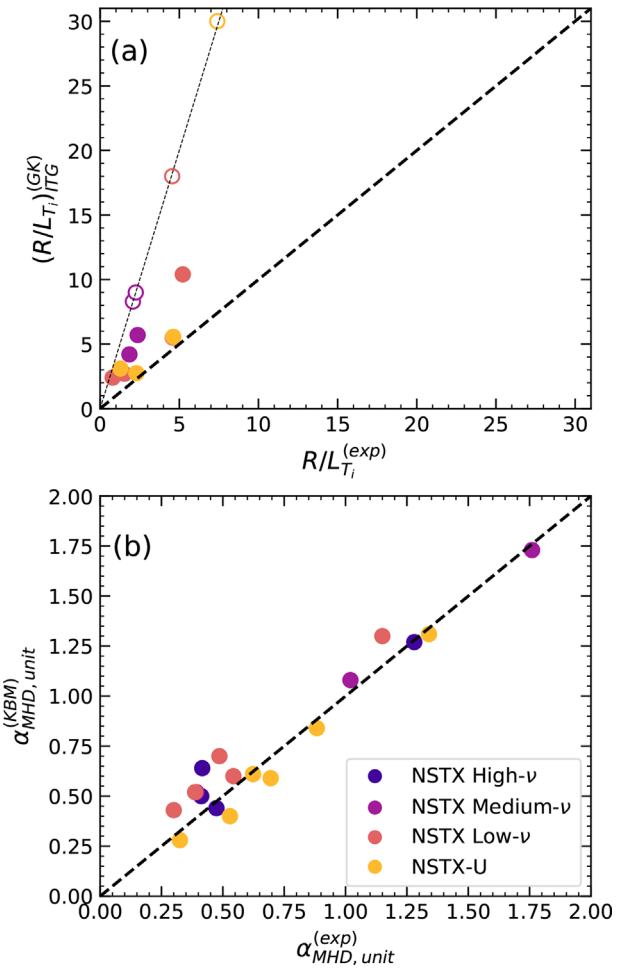

FIG. 22. Summary of (a) ITG and (b) KBM thresholds against the corresponding experimental value. The figure summarizes the thresholds of all the discharges and radial positions investigated. The dashed line indicates the condition in which the threshold is equal to the experimental value. Open symbols in (a) indicate that after increasing the ion temperature gradient four times, no ITG threshold were found.

low aspect ratio, high beta equilibria achievable in NSTX/NSTX-U. On the other hand, NSTX experimental profiles at many radii are very close to the KBM instability thresholds, as indicated by the dashed line in Fig. 22(b). For the NSTX-U case, the projected profiles also lie very close to the KBM stability threshold at all radii investigated ($r/a = 0.4$–0.9). The proximity of various discharges to the KBM instability thresholds implies that it may play an important role in limiting global energy confinement. However, it remains to be understood and predicted how KBM contributes to multi-channel transport (thermal and particle transport, for both ions and electrons) in a way that is consistent with experimental interpretation.

ACKNOWLEDGMENTS

This work is supported by the U.S. Department of Energy, Office of Science, under Award Nos. DE-SC0021385 and DE-SC0013977. The authors acknowledge Ron Bell, Ben LeBlanc, and the NSTX-U scientists who helped make the experimental profile measurements.

AUTHOR DECLARATIONS

Conflict of Interest

The authors have no conflicts to disclose.

Author Contributions

C. F. Clauser: Formal analysis (equal); Investigation (equal); Visualization (equal); Writing – original draft (equal); Writing – review & editing (equal). **W. Guttenfelder:** Conceptualization (equal); Methodology (equal); Supervision (equal); Writing – original draft (equal); Writing – review & editing (equal). **T. Rafiq:** Conceptualization (equal); Methodology (equal); Supervision (equal); Writing – original draft (equal); Writing – review & editing (equal). **E. Schuster:** Project administration (equal); Supervision (equal); Writing – review & editing (equal).

DATA AVAILABILITY

The data that support the findings of this study are openly available in Princeton Plasma Physics Laboratory DataSpace at http://arks.princeton.edu/ark:/88435/dsp01ng451m72r, Ref. 41.

APPENDIX: SUMMARY OF SOME CGYRO PARAMETERS

A brief summary of some of the CGYRO definitions used in this work is presented here in order to facilitate them for the reader. They are all defined in Refs. 14 and 27.

An important parameter used in this work is $\alpha_{MHD,unit}$. This parameter is a generalization of the standard definition

$$\alpha_{\mathrm{MHD}} = -q^2 R_0 \frac{8\pi}{B_0^2}\frac{dp}{dr}, \tag{A1}$$

in which B_0 is replaced by the effective magnetic field strength $B_{unit} = (q/r)d\psi/dr$ (which is a flux function). In addition, an effective pressure can be defined as

$$\beta^* = -\frac{8\pi}{B_{unit}^2}\frac{dp}{dr}. \tag{A2}$$

Here $p = \sum_s n_s T_s$ is the total pressure. Defining the temperature and density gradient scale lengths as $a/L_{T_s} = (a/T_s)dT_s/dr$ and $a/L_{n_s} = (a/n_s)dn_s/dr$, respectively, it is possible to write

$$\alpha_{\mathrm{MHD,unit}} = q^2 R_0 \beta_{e,unit} \sum_s \frac{p_s}{p_e}\left(\frac{a}{L_{T_s}} + \frac{a}{L_{n_s}}\right), \tag{A3}$$

where $\beta_{e,unit} = 8\pi n_e T_e / B_{unit}^2$. When a numerical equilibrium is read, quantities such as a/L_{T_s}, a/L_{n_s}, $\beta_{e,unit}$, and β^* (which are of interest in this work) are calculated from the equilibrium and they all satisfy Eqs. (A2) and (A3). In particular, among these parameters, only β^* affects the equilibrium calculation. However, CGYRO allows the user to scale these quantities in an independent way. As an example, one can change normalized temperature or density gradients without changing the effective pressure or β^* parameter and, therefore, keep the same equilibrium. This procedure can result in inconsistencies since Eq. (A2) might not be satisfied. However, since these quantities affect the gyrokinetic equations in different ways, it is customary to apply this technique to study different effects (see for example, Ref. 5).

In this work some scans over a/L_{T_s}, a/L_{n_s}, $\beta_{e,unit}$ are represented as a variation over the $\alpha_{MHD,unit}$ parameter. To do this, Eq. (A3) is invoked.

REFERENCES

[1]S. M. Kaye, R. E. Bell, D. Gates, B. P. LeBlanc, F. M. Levinton, J. E. Menard, D. Mueller, G. Rewoldt, S. A. Sabbagh, W. Wang, and H. Yuh, Phys. Rev. Lett. **98**, 175002 (2007).
[2]S. Kaye, F. Levinton, D. Stutman, K. Tritz, H. Yuh, M. Bell, R. Bell, C. Domier, D. Gates, W. Horton, J. Kim, B. LeBlanc, N. Luhmann, R. Maingi, E. Mazzucato, J. Menard, D. Mikkelsen, D. Mueller, H. Park, G. Rewoldt, S. Sabbagh, D. Smith, and W. Wang, Nucl. Fusion **47**, 499 (2007).
[3]Y.-K. Peng and D. Strickler, Nucl. Fusion **26**, 769 (1986).
[4]G. Rewoldt, W. M. Tang, S. Kaye, and J. Menard, Phys. Plasmas **3**, 1667 (1996).
[5]C. Bourdelle, W. Dorland, X. Garbet, G. W. Hammett, M. Kotschenreuther, G. Rewoldt, and E. J. Synakowski, Phys. Plasmas **10**, 2881 (2003).
[6]J. Y. Kim, W. Horton, and J. Q. Dong, Phys. Fluids B **5**, 4030 (1993).
[7]T. S. Hahm, K. H. Burrell, C. M. Greenfield, and E. J. Synakowski, Plasma Phys. Controlled Fusion **40**, 657 (1998).
[8]W. Guttenfelder, J. Candy, S. M. Kaye, W. M. Nevins, E. Wang, R. E. Bell, G. W. Hammett, B. P. LeBlanc, D. R. Mikkelsen, and H. Yuh, Phys. Rev. Lett. **106**, 155004 (2011).
[9]W. Guttenfelder, J. Peterson, J. Candy, S. Kaye, Y. Ren, R. Bell, G. Hammett, B. LeBlanc, D. Mikkelsen, W. Nevins, and H. Yuh, Nucl. Fusion **53**, 093022 (2013).
[10]J. Menard, S. Gerhardt, M. Bell, J. Bialek, A. Brooks, J. Canik, J. Chrzanowski, M. Denault, L. Dudek, D. Gates, N. Gorelenkov, W. Guttenfelder, R. Hatcher, J. Hosea, R. Kaita, S. Kaye, C. Kessel, E. Kolemen, H. Kugel, R. Maingi, M. Mardenfeld, D. Mueller, B. Nelson, C. Neumeyer, M. Ono, E. Perry, R. Ramakrishnan, R. Raman, Y. Ren, S. Sabbagh, M. Smith, V. Soukhanovskii, T. Stevenson, R. Strykowsky, D. Stutman, G. Taylor, P. Titus, K. Tresemer, K. Tritz, M. Viola, M. Williams, R. Woolley, H. Yuh, H. Zhang, Y. Zhai, and A. Zolfaghari, Nucl. Fusion **52**, 083015 (2012).
[11]S. Kaye, S. Gerhardt, W. Guttenfelder, R. Maingi, R. Bell, A. Diallo, B. LeBlanc, and M. Podesta, Nucl. Fusion **53**, 063005 (2013).
[12]See http://nstx-u.pppl.gov/ for "The NSTX-U 5-year research plan."
[13]F. Scotti, V. Soukhanovskii, R. Bell, S. Gerhardt, W. Guttenfelder, S. Kaye, R. Andre, A. Diallo, R. Kaita, B. LeBlanc, and M. Podestá, Nucl. Fusion **53**, 083001 (2013).
[14]J. Candy, E. Belli, and R. Bravenec, J. Comput. Phys. **324**, 73 (2016).
[15]GACODE Suite, https://gafusion.github.io/doc/index.html.
[16]H. Sugama, T.-H. Watanabe, and M. Nunami, Phys. Plasmas **16**, 112503 (2009).

[17]R. Arbon, J. Candy, and E. A. Belli, Plasma Phys. Controlled Fusion **63**, 012001 (2021).
[18]J. Candy, Plasma Phys. Controlled Fusion **51**, 105009 (2009).
[19]R. E. Waltz and R. L. Miller, Phys. Plasmas **6**, 4265 (1999).
[20]These features are not meant to be a full description of a mode, but they are the ones that were used to find them in this study.
[21]D. Hatch, M. Kotschenreuther, S. Mahajan, P. Valanju, F. Jenko, D. Told, T. Görler, and S. Saarelma, Nucl. Fusion **56**, 104003 (2016).
[22]W. Guttenfelder, J. Candy, S. M. Kaye, W. M. Nevins, E. Wang, J. Zhang, R. E. Bell, N. A. Crocker, G. W. Hammett, B. P. LeBlanc, D. R. Mikkelsen, Y. Ren, and H. Yuh, Phys. Plasmas **19**, 056119 (2012).
[23]H. Doerk, F. Jenko, M. J. Pueschel, and D. R. Hatch, Phys. Rev. Lett. **106**, 155003 (2011).
[24]J. W. Connor, R. J. Hastie, and A. Zocco, Plasma Phys. Controlled Fusion **55**, 125003 (2013).
[25]P. W. Terry, D. Carmody, H. Doerk, W. Guttenfelder, D. R. Hatch, C. C. Hegna, A. Ishizawa, F. Jenko, W. M. Nevins, I. Predebon, M. J. Pueschel, J. S. Sarff, and G. G. Whelan, Nucl. Fusion **55**, 104011 (2015).
[26]M. Kotschenreuther, W. Dorland, Q. Liu, M. Zarnstorff, R. Miller, and Y. Lin-Liu, Nucl. Fusion **40**, 677 (2000).
[27]E. A. Belli and J. Candy, Phys. Plasmas **17**, 112314 (2010).
[28]M. Kotschenreuther, X. Liu, D. Hatch, S. Mahajan, L. Zheng, A. Diallo, R. Groebner, J. Hillesheim, C. Maggi, C. Giroud, F. Koechl, V. Parail, S. Saarelma, E. Solano, and A. Chankin, Nucl. Fusion **59**, 096001 (2019).
[29]W. Guttenfelder, J. Candy, S. M. Kaye, W. M. Nevins, R. E. Bell, G. W. Hammett, B. P. LeBlanc, and H. Yuh, Phys. Plasmas **19**, 022506 (2012).
[30]T. Rafiq, S. Kaye, W. Guttenfelder, J. Weiland, E. Schuster, J. Anderson, and L. Luo, Phys. Plasmas **28**, 022504 (2021).
[31]E. A. Belli and J. Candy, Phys. Plasmas **25**, 032301 (2018).
[32]F. Romanelli, Phys. Fluids B **1**, 1018 (1989).
[33]F. Jenko, W. Dorland, and G. W. Hammett, Phys. Plasmas **8**, 4096 (2001).
[34]S. Gerhardt, R. Andre, and J. Menard, Nucl. Fusion **52**, 083020 (2012).
[35]K. Aleynikova and A. Zocco, Phys. Plasmas **24**, 092106 (2017).
[36]D. Told, F. Jenko, P. Xanthopoulos, L. D. Horton, and E. Wolfrum, Phys. Plasmas **15**, 102306 (2008).
[37]J. F. Parisi, F. I. Parra, C. M. Roach, C. Giroud, W. Dorland, D. R. Hatch, M. Barnes, J. C. Hillesheim, N. Aiba, J. Ball, P. G. Ivanov, and J. Contributors, Nucl. Fusion **60**, 126045 (2020).
[38]D. J. Battaglia, W. Guttenfelder, R. E. Bell, A. Diallo, N. Ferraro, E. Fredrickson, S. P. Gerhardt, S. M. Kaye, R. Maingi, and D. R. Smith, Phys. Plasmas **27**, 072511 (2020).
[39]M. Coury, W. Guttenfelder, D. R. Mikkelsen, J. M. Canik, G. P. Canal, A. Diallo, S. Kaye, G. J. Kramer, and R. Maingi, Phys. Plasmas **23**, 062520 (2016).
[40]W. Guttenfelder, R. Groebner, J. Canik, B. Grierson, E. Belli, and J. Candy, Nucl. Fusion **61**, 056005 (2021).
[41]C. F. Clauser (2022). "Linear ion-scale micro-stability analysis of high and low-collisionality NSTX discharges and NSTX-U projections," DataSpace. http://arks.princeton.edu/ark:/88435/dsp01ng451m72r.